UNIVERSITY OF CALIFORNIA SAN DIEGO

Barrier Layers and Metal Fill for Back End of Line Processing

A dissertation submitted in partial satisfaction of the requirements for the degree Doctor of Philosophy

in

Materials Science and Engineering

by

Steven Frank Wolf

Committee in Charge:

Professor Andrew C. Kummel, Chair
Professor Yeshaiahu Fainman
Professor David Fenning
Professor Ivan Schuller
Professor Wei Xiong

2019

The Dissertation of Steven Frank Wolf is approved, and it is acceptable in quality and form for publication on microfilm and electronically:

Chair

University of California San Diego

2019

DEDICATION

To my mother, Annette, and father, Doug, whose steadfast encouragement has pushed my desire to succeed. Thank you for the unwavering support.

EPIGRAPH

It’s not whether you get knocked down; it’s whether you get up.

Vince Lombardi

TABLE OF CONTENTS

LIST OF SYMBOLS AND ABBREVIATIONS

A	ampere
Å	angstrom
AFM	atomic force microscopy
ALD	atomic layer deposition
BE	binding energy
BEOL	back-end-of-line
BCl_3	boron trichloride
BN	boron nitride
Co	cobalt
$Co(dad)_2$	Bis(1,4-di-tert-butyl-1,3-diazadienyl) cobalt
cm^2	square centimeter
Cu	copper
CVD	chemical vapor deposition
eV	electron volt
h	Planck's constant
HCOOH	formic acid
HOPG	highly ordered pyrolytic graphite
HV	high vacuum
KE	kinetic energy
L	Langmuir
ML	megaLangmuir
MOSCAP	metal oxide semiconductor capacitor

MOSFET	metal oxide semiconductor field effect transistor
NH_3	ammonia
N_2H_4	hydrazine
nm	nanometer
pA	picoamps
PBN	pyrolitic boron nitride
PDA	post-deposition anneal
PEALD	plasma enhanced atomic layer deposition
PVD	physical vapor deposition
Ru	ruthenium
$RuDMBD(CO)_3$	η^4-2,3-dimethylbutadiene ruthenium tricarbonyl
SEM	scanning electron microsocopy
SiGe	silicon germanium
SiO_2	silicon dioxide
SPM	scanning probe microscopy
SRC	Semiconductor Research Corporation
STM	scanning tunneling microscopy
STS	scanning tunneling spectroscopy
TaN_x	tantalum nitride
TBA	tertiary butylamine
TBTDET	tris(diethylamido)(tert-butylimido) tantalum
TDMAT	tetrakis (dimethylamido) titanium
TEM	transmission electron microscopy

$TiCl_4$	titanium tetrachloride
TiN_x	titianium nitride
TMD	transition metal dichalcogenide
UHV	ultra high vacuum
V	volts
XPS	x-ray photoelectron spectroscopy
μ	micro
υ	frequency
Φ_{spec}	spectrometer work function

LIST OF FIGURES AND TABLES

ACKNOWLEDGEMENTS

I would like to first recognize my advisor, Professor Andrew Kummel, who has been a very direct, open, and readily available source of much knowledge and experience. He has provided many opportunities to develop myself into a motivated engineer by allowing me to present my work at several conferences every year, including an international symposium in Taiwan. His guidance and direction has allowed me to complete this incredible journey.

Dr. Tyler Kent and Dr. Mary Edmonds were two great senior graduate students in the Kummel group who essentially trained me and provided the most direction for achieving success in the program. They spent many hours of their time helping with data discussion and analysis, as well as helping me prepare for weekly group meeting presentations and conference presentations. Additionally, they taught me everything that they knew about vacuum science and maintaining the chamber with little downtime. Overall, I will never forget their contributions to directing me to become a successful student in the Kummel lab. The time spent with both of them whom I consider friends will not be forgotten. Dr. Jun Hong Park and Dr. Kasra Sardashti are two others that I really must thank, as well. Dr. Park offered much guidance in STM and STS data collection. In addition, he always offered assistance in making paper quality figures. Dr. Sardashti was always willing to help experimentally, whether it was a sample that needed AFM scanning, or a MOSCAP that needed fabricating or measuring; he was always willing to do so.

I need to also thank Mike Breeden, a fellow colleague and friend that I have gotten to work with for over 2 years. He has been a valuable contributor to the Kummel

lab. He tremendously assisted operating the chamber, running ALD, performing XPS, and being able to do numerous measurements and fabrications at Nano3 that have been critical for our success. He has turned into a great student, and I know that he will see his hard work continue to pay off in the future.

More recently, other fellow colleagues that I have worked with have became very close friends. Scott Ueda, Jong Choi, Chris Ahles, and Victor Wang have been the best group of people to work with on a day in, day out basis, as well as outside of work. They always have been there to assist me not only in my work, but helping out with my dogs when they needed watching, running the AVS 5k together, or even just enjoying a stress-relieving workout together. The memories in and out of lab with these people will never be forgotten and really made my time in San Diego a positive, enjoyable experience.

I must also give a thanks to all the other Kummel group members whom I have had the pleasure of attending conferences with, taking classes with, working with, and enjoying our weekly group meetings with: Dr. Sang Wook Park, Dr. Iljo Kwak, Dr. Natalie Mendez, Dr. Alex Liberman, Dr. Evgeniy Chagarov, Dr. Mahmut Kavrik, James Wang, Aaron Mcleod, and Yunil Cho. Thanks to Sofia Clemente, Jennie Chen, Kristen Ithikara, and Heather Sears who helped a lot over the years with lab purchase orders and trip coordination and reimbursement. Lastly, the folks at the machine shop have assisted my research tremendously when it comes to helping with designing new equipment and being able to help ease mistakes that were made in the lab at unfortunate times.

I have enjoyed collaborations with many industrial supporters such as Applied Materials, Rasirc, BASF, and most importantly, the SRC. Dan Alvarez, Russ Holmes, and Jeff Spiegelman from Rasirc really helped Dr. Edmonds and I with precursor and

purifier setups along with valuable discussions with N_2H_4 results. They were great colleagues to learn from and work with over the years.

I want to thank my committee members for being involved in my senate and dissertation defense presentations. My committee includes Professor David Fenning, Professor Yeshaiahu Fainman, Professor Ivan Schuller, and Professor Wei Xiong.

Melissa Hernandez and her family deserve much credit for driving me down this path; without her and them I would never have seen myself grow to what I am now. Most importantly though, I want to give thanks for the continuous support from my family: Doug, Annette, Tyler, and Courtney Wolf, as well as all extended Wolf, Denning, Durham, and Jonke family. All of you have always been there for me throughout school and life no matter the circumstance. Each of you means so much to me! Lastly, my dogs, Tucker and Tyson, and have been a daily source of happiness that made the tough times feel not so bad. No matter how crazy you two are, I will always take care of you.

Many companies throughout the years funded this work. These companies included Applied Materials, TSMC, Rasirc, BASF, and the SRC; all of them whose contributions allowed my research to thrive.

Chapter 2, in part or in full, is a reprint of the material as it appears in the Journal of Applied Surface Science: S. Wolf, M. Edmonds, K. Sardashti, M. Clemons, J. Park, N. Yoshida, L. Dong, R. Holmes, D. Alvarez, and A. Kummel. "Low-Temperature Amorphous Boron Nitride on $Si_{0.7}Ge_{0.3}$(001), Cu, and HOPG from Sequential Exposures of N_2H_4 and BCl_3." Applied Surface Science. (2018). The dissertation author was the primary investigator and author of this paper.

Chapter 3, in part or in full, is reprinted with permission from S. Wolf, M. Breeden, I. Kwak, J. H. Park, M. Kavrik, M. Naik, D. Alvarez, J. Spiegelman, and A. Kummel. "Low-Temperature Thermal ALD TaN_x and TiN_x from Anhydrous N_2H_4." Applied Surface Science. (2018). The dissertation author was the primary investigator and author of this paper.

Chapter 4, is in part or full, reprinted with permission from S. Wolf, M. Breeden, S. Ueda, J. Woodruff, M. Moinpour, R. Kanjolia, A. C. Kummel, "The Role of Oxide Formation on Selective Co and Ru Metal ALD" (*manuscript submitted to Applied Surface Science)*. The dissertation author was the primary investigator and author of this paper.

VITA

EDUCATION

2014 Bachelor of Science in Chemical Engineering, University of New Mexico

2015 Master of Science in Materials Science and Engineering, University of California San Diego

2019 Doctor of Philosophy in Materials Science and Engineering, University of California San Diego

PUBLICATIONS

S. Wolf, M. Breeden, I. Kwak, J. H. Park, M. Kavrik, M. Naik, D. Alvarez, J. Spiegelman, and A. Kummel. "Low-Temperature Thermal ALD TaN_x and TiN_x from Anhydrous N_2H_4." *Applied Surface Science*. *(2018)*.

S. Wolf, M. Edmonds, K. Sardashti, M. Clemons, J. Park, N. Yoshida, L. Dong, R. Holmes, D. Alvarez, and A. Kummel. "Low-Temperature Amorphous Boron Nitride on $Si_{0.7}Ge_{0.3}$(001), Cu, and HOPG from Sequential Exposures of N_2H_4 and BCl_3." *Applied Surface Science*. *(2018)*.

S. Wolf, M. Edmonds, K. Sardashti, M. Clemons, E. Yieh, S. Nemani, R. Holmes, D. Alvarez, and A. Kummel. "Sequential N_2H_4 + BCl_3 Exposures on $Si_{0.7}Ge_{0.3}$(001) and HOPG". *TechCon*. *(2017)*.

S. Wolf, M. Edmonds, X. Jiang, R. Droopad, B. Sahu, S. S. Siddiqui and A. Kummel "Rapid In-Situ Carbon and Oxygen Cleaning of $In_{0.53}Ga_{0.47}As$(001) and $Si_{0.5}Ge_{0.5}$(110) Surfaces via a H_2 RF Downstream Plasma" *ECS Transactions 72(4):291-302 (2016)*.

J.H. Park, S. Vishwanath, S. Wolf, K. Zhang, I. Kwak, M. Edmonds, M. Breeden, X. Liu, M. Dobrowolska, J. Furdyna, J.A. Robinson, H.G. Xing and A.C. Kummel "Selective Chemical Response of Transition Metal Dichalcogenides and Metal Dichalcogenides in Ambient Conditions " ACS Appl. Mater. Interfaces 9, 29255 (2017).

C.F. Ahles, J.Y. Choi, S. Wolf, and A.C. Kummel "Selective Etching of Silicon in Preference to Germanium and Si0.5Ge0.5" ACS Appl. Mater. Interfaces 9, 20947 (2017).

C.F. Ahles, J.Y. Choi, S. Wolf, A.C. Kummel "Selective Etching of Silicon in Preference to Germanium and $Si_{0.5}Ge_{0.5}$" *Proceedings of VLSI-TSA (2017)*.

M. Edmonds, S. Wolf, E. Chagarov, T. Kent, J.H. Park, R. Holmes, D. Alvarez, R. Droopad, A.C. Kummel "Self-limiting CVD of a passivating SiO_x control layer on InGaAs(001)-(2x4) with the prevention of III-V oxidation" *Surf. Sci. 660, 31-38 (2017).*

M. Edmonds, K. Sardashti, S. Wolf, E. Chagarov, M. Clemons, T. Kent, J.H. Park, K. Tang, P.C. McIntyre, N. Yoshida, L. Dong, R. Holmes, D. Alvarez, and A.C. Kummel "Low Temperature Thermal ALD of an SiNx interfacial diffusion barrier and surface passivation layer on $SixGe_{1-x}$(001)/(110) surfaces" *J. Chem Phys 146, 052820 (2016).*

D. Alvarez, J. Spiegelman, A. Kummel, M. Edmonds, K. Sardashti, S. Wolf, and R. Holmes" Surface Passivation of New Channel Materials Utilizing Hydrogen Peroxide and Hydrazine Gas" *Solid State Phenomena 255, pp 31-35 (2016).*

M. Edmonds, T.J. Kent, S. Wolf, K. Sardashti, M. Chang, J. Kachian, R. Droopad, E. Chagarov, A. Kummel. "In0.53Ga0.47As(001)−(2x4) and $Si_{0.5}Ge_{0.5}$(110) surface passivation by self-limiting deposition of silicon containing control layers" *International Symposium on VLSI Technology, Systems and Application (VLSI-TSA). (2016).*

J.H. Park, S. Fathipour, I. Kwak, K. Sardashti, S. Wolf, C. Ahles, S. Vishwanath, H. G. Xing, S. K. Fullerton- Shirley,A. Seabaugh A. C. Kummel "Atomic Layer Deposition of Al_2O_3 on WSe_2 Functionalized by Titanyl Phthalocyanine. *ACS Nano* 10.7 *(2016)*.

FIELD OF STUDY

Major Field: Materials Science and Engineering

Studies in Surface Science and Thin Film Atomic Layer Deposition
Professor Andrew C. Kummel

ABSTRACT OF THE DISSERTATION

Barrier Layers and Metal Fill for Back End of Line Processing

by

Steven Frank Wolf

Doctor of Philosophy in Materials Science and Engineering

University of California San Diego, 2019

Professor Andrew C. Kummel, Chair

As semiconductor devices continue to scale down below the 10 nm node, deposition of conformal, ultra-thin layers on high aspect ratio features becomes very challenging. As such, there is a need to deposit these materials with precise thickness and stoichiometry control via atomic layer deposition (ALD). Two main applications for ALD occur during BEOL microelectronic device processing after the MOSFET has been fabricated: barrier layer deposition and interconnect fill. These two applications will be the focus of this dissertation. ALD barrier layers are typically conductive nitrides, as such, this work will discuss growing several nitrides with ALD using N_2H_4 which has the

main advantage of being able to grow at lower deposition temperatures. Commonly used barrier layers, titanium nitride (TiN) and tantalum nitride (TaN) have been extensively studied in devices because of their ideal thermal, mechanical, and electrical properties and ability to act as metal diffusion barriers, but typically require high deposition temperatures due to using less reactive NH_3 as the N-containing precursor. Additionally, amorphous boron nitride was explored due to it having shorter bonds than TiN and TaN potentially making it a more-effective diffusion barrier that could be scaled down to films that must be less than 5 nm thick. These three materials in particular will be the focus in Chapters 2 and 3.

Deposition of conductive interconnect metal in shrinking vias is another common problem facing the microelectronics industry. Traditionally, Al and then Cu have been used due to their high conductivities; however, in small critical dimensions, the resistivity of Cu increases due to electron scattering. Therefore, new materials and processing conditions are being explored that can offer lower resistivity for interconnect fill in these small critical dimension features. Chapter 4 of this dissertation will discuss two selective ALD processes (Co and Ru) that can allow for bottom-up fill of the interconnect metal. This would induce the formation and growth of larger grains, which are expected to decrease via and interconnect resistance. Reducing grain boundaries and decreasing surface roughness achieve this. For the analysis and characterization of ALD films, *in situ* XPS and STM along with *ex situ* AFM were mainly employed to characterize the chemical, electrical and topographical features of the deposited films and surfaces. To further study the conductivity of films, *ex situ* four-point probe measurements were performed.

Chapter 1

Introduction

1.1 Microelectronic Device Scaling

In order to keep up with Moore's Law, microelectronic devices have to keep shrinking to increase the number of transistors in a limited area. Currently, device scaling has reached the sub-nanometer regime requiring Angstrom (Å) level precision when depositing films particularly on high aspect ratio features used in current device architectures. As a result, more conventional deposition techniques with less processing control in the nanometer regime, such as CVD and PVD (chemical and physical vapor deposition) are now in competition with ALD. ALD can achieve conformal ultra-thin film deposition by alternating exposure to various precursors in a sequential manner typically at a lower growth temperature (< 400°C), which is advantageous for back-end-of-line (BEOL) applications (*1, 2*).

The goal of this dissertation is to describe novel ALD processes that were developed that can produce suitable films that can replace technology that is currently being utilized in industry. For instance, for barrier layer applications, conductive metal nitrides are deposited with plasma-enhanced processes (*3-6*). By using a more reactive N-containing source (N_2H_4), a thermal ALD process can produce desirable films at lower temperature with good film nucleation. In particular, three ALD nitrides—BN, TiN, and TaN and the corresponding growth conditions, film characteristics, and applications will be discussed in the subsequent chapters. Additionally, being able to deposit novel metals for interconnect applications has become a big area of focus during BEOL processing. Co

and Ru metal are replacing Cu at small feature sizes due to their ability to have improved conductivities (*7, 8*). Moreover, depositing these materials via a selective process can allow for the films to grow bottom-up, a desirable result that can lead to less surface roughness and grain boundaries that can ultimately lead to an improvement in conductivity.

1.2 ALD Processing Fundamentals

Most ALD procedures consist of two half-reactions, in which each precursor is separately and sequentially dosed onto the sample in vacuum. Each half-reaction self-limits, and ideally one monolayer of the desired ALD material is deposited after one complete cycle. To prevent CVD and unwanted byproduct reactions from occurring, purges with an inert gas must succeed each half cycle; therefore, a typical ALD cycle is performed as follows: precursor A is exposed to the sample surface, a purge with an inert gas is ran to remove unreacted precursor and reaction byproducts, precursor B is exposed, and lastly, a inert gas purge is ran again to remove byproducts and excess precursor. Numerous cycles can then be performed to achieve a desired film thickness. As an example, Figure 1.1 outlines the ALD procedure for BN using N_2H_4 (precursor A) and BCl_3 (precursor B).

Several ALD processes were developed based on their CVD counterparts and normally have an ALD temperature window in which they are operated. If the temperature is too low, poor growth is achieved due to slow reaction kinetics or precursor condensation. If the temperature is too high, the precursors can decompose and become

unreactive or desorption from the surface can overwhelm (*9, 10*). Surface temperatures are typically less than 400°C in order to achieve ideal growth rates, typically near 1 Å. In a similar manner to operating within the ALD temperature window, precursor exposure conditions must be determined as well. Lastly, along with surface temperature and precursor exposure time, surface termination is another crucial parameter that can dictate the reactivity of various surfaces to ALD reactions. This last parameter has been explored and has grown into the field of selective area deposition (*11-13*).

1.3 Ultra High Vacuum Chamber

For the work presented in this dissertation, an Omicron variable temperature ultra-high vacuum (UHV) chamber equipped with a monochromatic X-ray photoelectron spectroscopy (XPS) system and scanning tunneling microscopy/spectroscopy (STM/STS) system was utilized. Two home-built ALD chambers were added to the Omicron system to be able to characterize the ALD without exposure to ambient conditions (Fig. 1.2 and Fig 4.2). Starting substrates (Si, SiO_2, Cu, Pt, etc) were characterized before and after cleaning and deposition by first placing them into a turbo-pumped load-lock chamber. After sufficient pump-down, the samples were moved into the UHV chamber. The two ALD chambers were turbo-pumped with rotary vane backed pumps and achieved base pressures of ~$1x10^{-7}$ torr. Both ALD chambers contained a manipulator for sample transfer and positioning which was equipped with a cartridge heater that was not inside the vacuum. This cartridge heater was an upgraded design from a prior pyrolytic boron nitride (PBN) heaters in which deposition would lead to shorting out the heater. After exposing samples to precursor gas or performing ALD cycles, the samples were

transferred back into the UHV chamber for characterization with XPS and STM/STS. The novelty of this multi-chamber HV/UHV system prevented any oxidation or surface contamination by eliminating air exposure prior to characterization.

To further elaborate on the system setup, various precursors were attached to the ALD chambers. Anhydrous N_2H_4, BCl_3, $TiCl_4$, $Co(dad)_2$, and any other precursor could readily be swapped on or off the chamber. One of the ALD chambers had a PIE downstream plasma source that could be used for cleaning samples or performing plasma-enhanced ALD (Fig 4.2). The UHV chambers were comprised of the XPS chamber and the Scanning Probe Microscopy (SPM) chamber. These two chambers were separated by a gate valve and both ion-pumped along with possessing the capability of firing the titanium sublimation getter pumps to achieve base pressures of $<2x10^{-10}$ Torr. The XPS chamber contained a manipulator equipped with a PBN heater for resistive annealing and heating, which would be used for performing sample cleans and PDAs. The XPS chamber also included a mass spectrometer, a thermal gas cracker, and an STM tip cracking wire. Lastly, there was sample and STM tip storage located in this chamber.

1.4 X-Ray Photoelectron Spectroscopy

XPS was the main characterization technique employed throughout this dissertation to study the chemical composition of the various surfaces. In addition to chemically characterizing the starting surface and after ALD, XPS could also be used for surface saturation studies and percent coverage estimations for the top ~5 nm of deposition. This monochromatic XPS system exposes a sample surface of interest with x-rays and core and valence electrons are ejected with discrete characteristic kinetic

energies. A series of lenses are used to specify the analysis area spot size which is ~750 μm in this system. A hemispherical multichannel analyzer collects the electrons, along with a set electron pass energy that applies voltages to retard or accelerate the collected electrons. To amplify the signal from the collected electrons, a 5-channel electron multiplier is used to amplify current by 10^8. This current is then fed to a preamplifier where the electron counts are recorded in the form of a spectrum. A very broad survey spectrum can be performed across a wide range of energies, or more high-resolution narrow scans can be achieved by shrinking the scan range and increasing the number of sweeps. The kinetic energy (KE) of the electrons are measured by the detector, but are translated to binding energy (BE) by subtracting the KE from for the incoming energy of the x-rays along with the work function of the spectrometer (Φ_{spec}) *(14)*. For the case of this system, which utilizes an Al-coated anode, the incoming energy, $E_{h\upsilon}$, is 1486.7 eV for Al K_α radiation.

The power of XPS lies with its ability to detect surface elemental chemical shifts. A chemical shift is a binding energy shift due to a change in chemical bonding that causes oxidation or reduction. This is accomplished by observing a shifted BE component (peak or shoulder) in the recorded spectrum. Typical shifts are on the order of ~4eV or less. Overall, the measurement capability of XPS can help in determining the chemical species present on the surface, the chemical stoichiometry and oxidation states, and give some estimation as to the thickness of the deposited ALD film based on the attenuation of the signal from the starting substrate.

1.5 Atomic Force Microscopy

Atomic Force Microscopy (AFM) was mainly used in this dissertation to characterize the surface topography of starting substrates and deposited films. AFM is a type of scanning probe microscopy with a high resolution to surface features (typically down to ~1nm and potentially even less depending on the quality of the tip).

During AFM, the tip is brought into contact with the sample and raster scanned along the x and y directions. A feedback loop, which utilizes the cantilever deflection as input, is employed to keep the probe-sample force constant during scanning. Ultimately, changes in height are measured by a photodiode recording the change in the deflection of the cantilever (Fig 1.3) *(15)*. AFM has the advantage that it is simple and efficient at studying ALD films when compared to other imaging technologies, such as SEM, TEM, and other optical microscopy techniques that either have to use lenses, electron beam irradiation, a high vacuum, or ultimately deliver low resolution. Therefore, AFM has proved a valuable imaging technique for this dissertation.

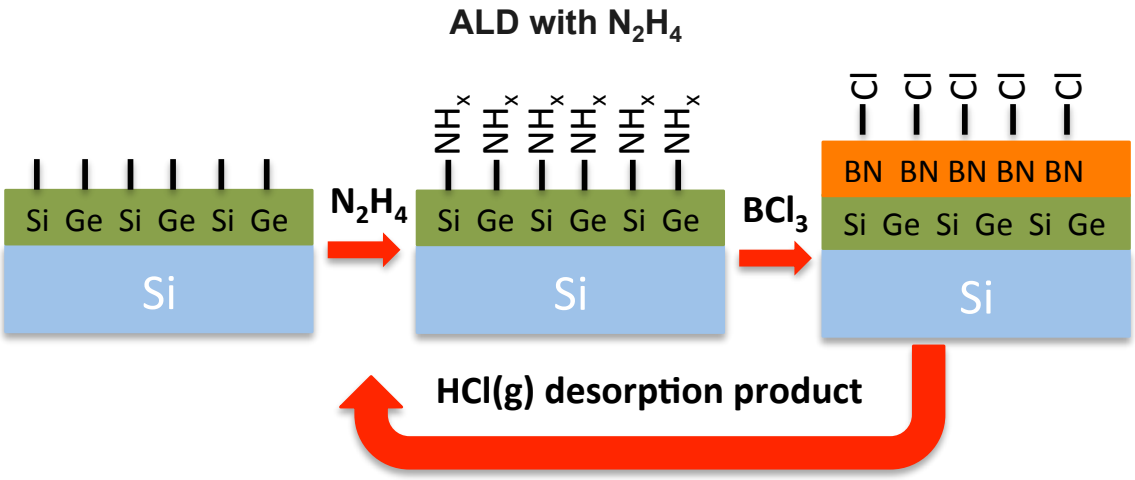

Figure 1.1: Example of BN ALD with N_2H_4 + BCl_3. The first half-cycle exposure of N_2H_4 terminates the surface with reactive NH_x species. After a pump and/or purge, BCl_3 is exposed to the surface. The result is BN with the formation of a volatile HCl(g) byproduct.

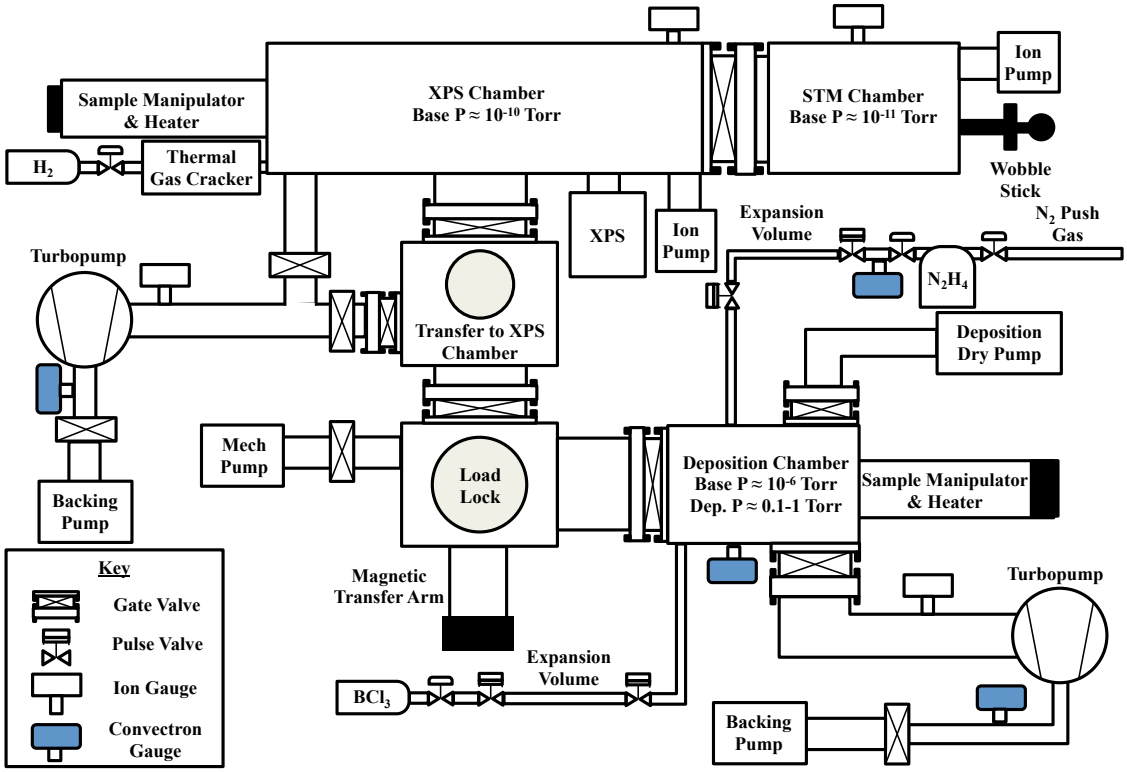

Figure 1.2: Chamber schematic. The system used for BN deposition was comprised of a load lock chamber, deposition chamber, XPS chamber, and STM chamber. After BN deposition, samples were transferred in vacuum without ambient exposure to perform *in situ* XPS and STM analysis.

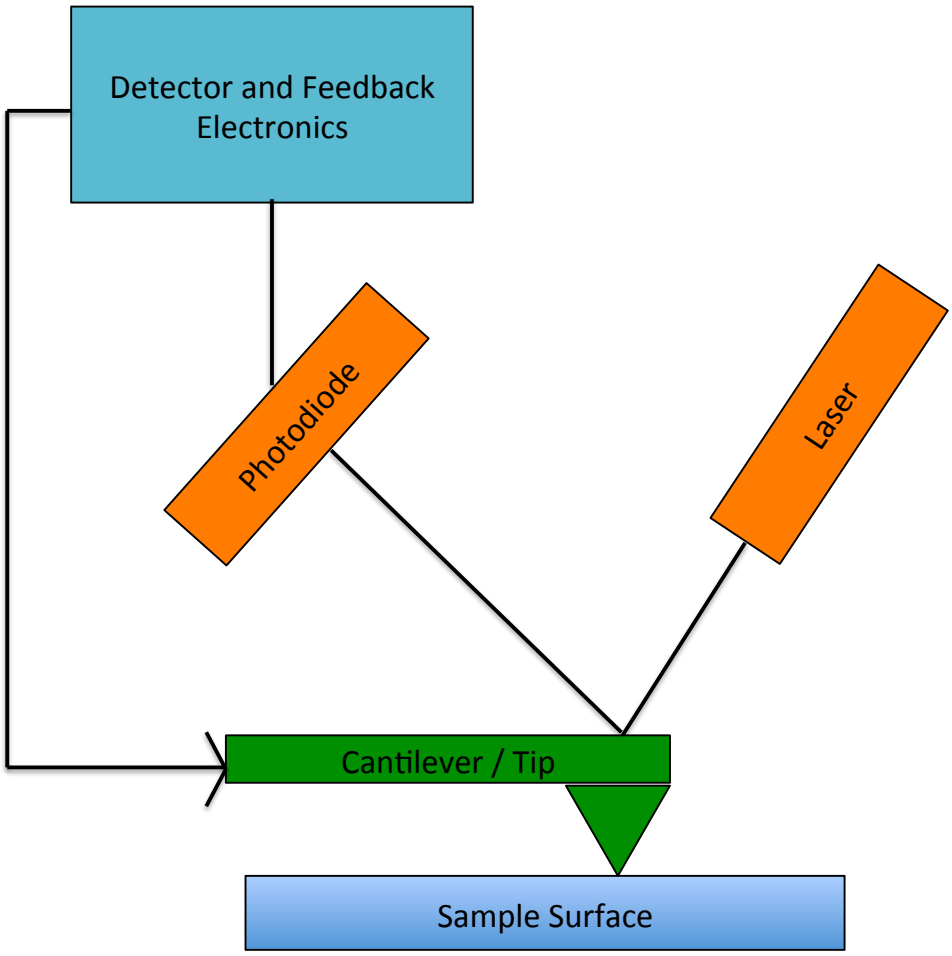

Figure 1.3: Details of AFM Operation. A tip is scanned across the sample surface and the change in height is recorded through the deflection of the cantilever. Feedback from the detector and electronics keep the tip in contact with the surface. Adapted from Binnig *et al (15)*.

1.6 References

1. M. Leskelä, M. Ritala, Atomic layer deposition (ALD): from precursors to thin film structures. *Thin solid films* **409**, 138-146 (2002).

2. A. Sherman, Chemical vapor deposition for microelectronics: principles, technology, and applications. (1987).

3. R. Kröger, M. Eizenberg, C. Marcadal, L. Chen, Plasma induced microstructural, compositional, and resistivity changes in ultrathin chemical vapor deposited titanium nitride films. *Journal of applied physics* **91**, 5149-5154 (2002).

4. K.-E. Elers, J. Winkler, K. Weeks, S. Marcus, TiCl4 as a precursor in the TiN deposition by ALD and PEALD. *Journal of the Electrochemical society* **152**, G589-G593 (2005).

5. Caubet, P., Blomberg, T., Benaboud, R., Wyon, C., Blanquet, E., Gonchond, J.P., Juhel, M., Bouvet, P., Gros-Jean, M., Michailos, J. and Richard, C. Low-temperature low-resistivity PEALD TiN using TDMAT under hydrogen reducing ambient. *Journal of The Electrochemical Society* **155**, H625-H632 (2008).

6. H.-S. Chung, J.-D. Kwon, S.-W. Kang, Plasma-enhanced atomic layer deposition of TaN thin films using tantalum-pentafluoride and N2⁄ H2⁄ Ar plasma. *Journal of The Electrochemical Society* **153**, C751-C754 (2006).

7. Wen, L.G., Adelmann, C., Pedreira, O.V., Dutta, S., Popovici, M., Briggs, B., Heylen, N., Vanstreels, K., Wilson, C.J., Van Elshocht, S. and Croes, K., in *2016 IEEE International Interconnect Technology Conference/Advanced Metallization Conference (IITC/AMC)*. (IEEE, 2016), pp. 34-36.

8. Bekiaris, N., Wu, Z., Ren, H., Naik, M., Park, J.H., Lee, M., Ha, T.H., Hou, W., Bakke, J.R., Gage, M. and Wang, Y., in *2017 IEEE International Interconnect Technology Conference (IITC)*. (IEEE, 2017), pp. 1-3.

9. G. N. Parsons, S. M. George, M. Knez, Progress and future directions for atomic layer deposition and ALD-based chemistry. *Mrs Bulletin* **36**, 865-871 (2011).

10. R. W. Johnson, A. Hultqvist, S. F. Bent, A brief review of atomic layer deposition: from fundamentals to applications. *Materials today* **17**, 236-246 (2014).

11. K. Park, J. Doub, T. Gougousi, G. Parsons, Microcontact patterning of ruthenium gate electrodes by selective area atomic layer deposition. *Applied Physics Letters* **86**, 051903 (2005).

12. R. Chen, H. Kim, P. C. McIntyre, D. W. Porter, S. F. Bent, Achieving area-selective atomic layer deposition on patterned substrates by selective surface modification. *Applied Physics Letters* **86**, 191910 (2005).

13. J. P. Klesko, M. M. Kerrigan, C. H. Winter, Low temperature thermal atomic layer deposition of cobalt metal films. *Chemistry of Materials* **28**, 700-703 (2016).

14. T. L. Barr, *Modern ESCAThe Principles and Practice of X-Ray Photoelectron Spectroscopy*. (CRC press, 1994).

15. Binnig, G., Quate, C. F., & Gerber, C. (1986). Atomic force microscope. *Physical review letters*, *56*(9), 930.

Chapter 2

Low-Temperature Amorphous Boron Nitride on $Si_{0.7}Ge_{0.3}$(001), Cu, and HOPG from Sequential Exposures of N_2H_4 and BCl_3

2.1 Abstract

Low-temperature sequential exposures of N_2H_4 and BCl_3 have been performed on $Si_{0.3}Ge_{0.7}$(001), Cu, and HOPG surfaces at 350°C. A novel BN ALD process has been achieved on $Si_{0.3}Ge_{0.7}$(001) with 60 cycles of BN ALD producing a uniform, pinhole-free thin film with low contamination, as characterized with XPS and AFM. On Cu and $Si_{0.3}Ge_{0.7}$(001), XPS spectra indicated a near stoichiometric BN film. While AFM imaging indicated the deposition on Cu yielded nanometer-scale etching, conformal deposition was observed on $Si_{0.3}Ge_{0.7}$(001). The BN ALD also nucleated on inert HOPG via step edges. *In situ* STM imaging showed that cyclic exposures at 350°C were able to decorate step edges with features ~2 nm tall and ~200 nm wide, indicating the propensity for BN to grow in the planar direction. The N_2H_4 and BCl_3 ALD allows for the deposition of low oxygen, low carbon films, but to avoid etching, the growth should be nucleated by N_2H_4, since exposure to BCl_3 can result in the formation of volatile Cl-containing surface species on many substrates. Therefore, the formation of a stable surface nitride prior to BCl_3 exposure is necessary to prevent formation and desorption of volatile species from the substrate.

2.2 Introduction

Boron nitride (BN) has gained attention due to its useful thermal and mechanical properties, chemical stability, wide bandgap, and ability to be deposited on a range of metallic and semiconducting surfaces *(1-5)*. BN has been utilized for applications ranging from high-temperature ceramics, protective coatings, and thin layers in semiconductor devices *(6-9)*. Recently, BN has been investigated for use as a low-k barrier layer on Cu, which is needed to reduce interconnect resistance-capacitance delays *(10)*. Amorphous BN forms shorter bonds in comparison to the more commonly used TaN and TiN barrier layers potentially making it a more effective barrier layer as device scaling continues. More prominently, though, hexagonal BN (hBN) has been extensively studied for use in 2D semiconductor devices, due to its structural similarity with graphene, chemical inertness, and lack of dangling bonds/surface traps, which make it a valuable low-k dielectric *(7, 11)* and substrate for TMD growth.

For the deposition of nitrides, most research has either focused on using thermal NH_3, which typically requires higher growth temperatures (in excess of 400°C), or using an activated source to lower the deposition temperature, such as plasma. However, this is accomplished at the expense of damage to the substrate. For BN, previous work has shown that BN atomic layer deposition with triethylborane and NH_3 with H_2 carrier gas occurs at 600°C-900°C with a growth rate of 0.7 Å/ cycle on sapphire and Si, but above this window, the process was not self-limiting *(12)*. George and colleagues demonstrated BN ALD with a growth rate of ~1 Å/ cycle with BCl_3 and NH_3 on ZrO_2 nanoparticles at 500K, but very large exposures in excess of 10^9 Langmuirs were required to saturate the half-cycle reactions *(4)*. Olander *et al.* demonstrated that growth with BBr_3 and NH_3

occurred at 400°C but with a growth rate of only 0.045 nm per cycle; laser-assisted ALD was required to achieve a growth rate closer to 0.1 nm per cycle *(13)*. For growth of hBN on 2D materials, chemical vapor deposition (CVD) is typically employed using higher temperatures (typically in the range of 650°C-1000°C) *(2, 14-17)*. As a result, developing a low-temperature ALD process with a reasonable growth rate for smaller precursor exposures would be advantageous on a variety of surfaces.

In this work, low-temperature plasma-less deposition of BN using sequential exposures of anhydrous hydrazine (N_2H_4) and boron trichloride (BCl_3) was performed on various substrates. A SiGe substrate was chosen since 1-2 monolayers of BN could act as a barrier for transition metal dichalcogenides (TMDs) grown on Si wafers or high mobility SiGe films on Si commercial wafers. TMDs deposited on Si have been shown to improve device performance *(18, 19)*. Cu was chosen since ultrathin diffusion barriers are needed *(10, 20, 21)*, and HOPG was chosen as a model of graphene for which 1-2 monolayer dielectrics are required *(7, 22)*. In addition, the diversity of surface reactivity enables a fundamental understanding of low-temperature BN ALD using N_2H_4 and BCl_3. By using anhydrous N_2H_4 as the reactive nitrogen source, the reaction with BCl_3 can proceed at a lower temperature than NH_3, while preventing oxygen incorporation into BN films, as previously demonstrated with SiN_x films *(23)*. Chloride-containing precursors, such as BCl_3, $TiCl_4$, Si_2Cl_6, are ideal for nitride ALD because of their favorable thermochemistry that induces an HCl(g) desorption product, ultimately leaving minimal unreacted Cl ligands in the deposited film. The contamination and excess Cl has been correlated with unfavorable properties in TiN films *(24, 25)*; therefore, maintaining a clean, nearly stoichiometric film is desirable. Furthermore, chlorine precursors can

induce etching via formation and desorption of volatile species (i.e. $SiCl_4$, Cu_3Cl_3), thereby roughening the substrate. In the present report, a self-limiting and saturating BN ALD occurred on $Si_{0.7}Ge_{0.3}$(001) with 60 cycles of BN ALD, which produced a uniform, nearly contamination-free film. The same precursors were sequentially exposed to Cu and HOPG substrates with the goal of achieving an ALD process, but the RMS surface roughness increase on Cu was consistent with precursor etching induced by the formation and desorption of volatile Cu species. On HOPG, nucleation was achieved at step edges with N_2H_4, and subsequent cycles of N_2H_4 and BCl_3 were performed at 350°C, leading to anisotropic growth in the planar direction. Ultimately, low oxygen, low carbon BN was deposited, but to avoid any etching by the precursors, the growth should be nucleated by N_2H_4 to form a stable surface nitride that can protect the surface from any etching caused by BCl_3.

2.3 Experimental

This study utilized 12 nm thick p-type $Si_{0.7}Ge_{0.3}$(001) that was epitaxially grown on a p-type Si(001) substrate (Applied Materials), 50 nm sputtered Cu on SiO_2/Si (Applied Materials), and HOPG purchased from SPI Supplies. $Si_{0.7}Ge_{0.3}$(001) samples underwent an *ex situ* wet clean involving a 10 minute sonication in acetone, a 10 minute sonication in isopropyl alcohol, a 5 minute sonication in DI water, followed by a 2 minute etch in 2% HF/H_2O. The samples were wetted with toluene to prevent surface oxidation before being loaded into the vacuum chamber with minimal air exposure. Once loaded into the UHV chamber (Fig. 1.1), the samples were heated to 330°C for 15 minutes and subsequently dosed with $1x10^{-6}$ Torr of atomic hydrogen for 30 minutes

(1800 Langmuirs) to remove surface carbon contamination. Atomic H was generated by flowing H_2 through a thermal gas cracker (Applied Research) operated at 65 W. The exposures were calculated for maximum cracking efficiency, but the actual efficiency was likely 30-50%. Cu samples were annealed in UHV at 350°C to drive off surface contamination, as well as dosed with atomic H to further remove contamination. HOPG was exfoliated with tape prior to being loaded into vacuum and subsequently annealed at 400°C for 30 minutes to remove physisorbed hydrocarbons from the surface.

Precursor exposures were performed in a deposition chamber that was separated from the UHV chamber by a gate valve (Fig. 1.1). The deposition chamber with attached precursor dosing lines was pumped by a turbomolecular pump that yielded a base pressure of 2×10^{-6} Torr. The entire chamber, precursor dosing lines, and connecting line to the dry pump were all continuously heated to 80-100°C to ensure both precursors would not condense to the chamber walls and react to form any solid powder byproduct. In addition, the N_2H_4 vessel was pressurized to atmospheric pressure with ultrahigh purity N_2 to act as a carrier gas. Note that reported N_2H_4/N_2 exposures below are reported as N_2H_4 exposures, and the actual N_2H_4 exposures are lower due to the dilution in N_2; from the vapor pressure of N_2H_4, the estimated fraction of N_2H_4 is approximately 1.5%. Samples were preheated in the UHV chamber before being transferred to the deposition chamber where they were radiatively heated by a PBN heater. After exposure to anhydrous N_2H_4 (Rasirc) and BCl_3 (Praxair), samples were transferred back to the UHV chamber where x-ray photoelectron spectroscopy (XPS) could be performed without breaking vacuum. An *in situ* monochromatic XPS system (Al kα hν = 1486.7 eV) was used to collect spectra at an angle of 30° with respect to the surface parallel, a pass

energy of 50 eV, and a line width of 0.1 eV. XPS analysis was conducted with CASA XPS v.2.3 and included Shirley background subtractions. Raw peak areas were corrected by Schofield photoionization cross sectional relative sensitivity factors. For Cu XPS spectra, the data was additionally corrected by the inelastic mean free paths due to the binding energy of Cu 2p being much larger than the other analyzed peaks. Along with *in situ* XPS, *in situ* scanning tunneling microscopy (STM) utilized constant current mode with a tip bias of +2V and current set point of 20 pA. Lastly, atomic force microscopy (AFM) was employed to image the surfaces.

2.4 Results and Discussion

2.4.1 $Si_{0.7}Ge_{0.3}(001)$

To determine the half-cycle dose sizes, as well as check for saturation dosing on $Si_{0.7}Ge_{0.3}(001)$, XPS was used to monitor successive exposures. Fig. 2.1 (a) shows the XPS corrected peak areas normalized to the sum of Si 2p and Ge 3d for the $Si_{0.7}Ge_{0.3}(001)$ surface. The surface was cleaned with 1800L atomic H at 330°C, followed by 5 cycles of 150 ML N_2H_4 and 150 ML BCl_3 to establish baseline N 1s and B 1s signals; the 5 ALD cycles terminated with a BCl_3 pulse. An additional 150 ML and 300 ML exposure of BCl_3 shows essentially no change in the B 1s signal, indicating saturation of the BCl_3 half-cycle. Similarly, 150 ML exposures of N_2H_4 (1/2 cycle ALD) followed by additional 300 ML exposures indicated the surface was nearly saturated after a total of 450 ML of N_2H_4 from the negligible increase in the N 1s signal during the last 300 ML N_2H_4 exposure; this confirmed the self-limiting ALD of BN on $Si_{0.7}Ge_{0.3}(001)$. It should be noted that the amount of Cl dropped from ~8% to ~2% after N_2H_4 dosing, but

was unable to be fully removed at a relatively low reaction temperature of 350ºC by large N_2H_4 exposures. At this sample temperature, saturated amounts of half-cycle exposures were crucial for maximizing ligand exchange on the surface to leave minimal Cl residue in the film.

After checking for saturation, thicker films were deposited using saturation pulses (300 ML BCl_3 + 450 ML N_2H_4 per ALD cycle). Fig. 2.2 (a) shows the XPS after 5, 30, and 60 cycles of BN on $Si_{0.7}Ge_{0.3}$(001) normalized to Si 2p + Ge 3d. Additionally, a final atomic H clean at 285°C for 20 minutes was performed to remove any remaining surface Cl. Fig. 2.2 (b) shows the raw Si 2p, B 1s, and N 1s peaks for the normalized data. The Si 2p peak attenuates, while the B 1s peak at ~190.5 eV and the N 1s peak at ~398 eV grow as a function of the number of cycles, in good agreement with previously reported binding energies *(26, 27)*. After 5 cycles, a broader N 1s peak was observed, which is indicative of the presence of an interfacial nitride between the boron nitride and $Si_{0.7}Ge_{0.3}$(001) surface. Note that the initial dosing by N_2H_4 formed this surface nitride, as evidenced by the higher binding energy component in the Si 2p region at ~101.7 eV, corresponding to an interfacial SiN_x. This interfacial SiN_x layer caused the deposited film to appear nitrogen-rich (B:N ratio = 0.45) after 5 ALD cycles of BCl_3 + N_2H_4 due to the Si-N bond formation detected in XPS. After 60 ALD cycles, the substrate Si 2p and Ge 3d peaks as well as interfacial SiN_x component were nearly fully attenuated; therefore; the ratio of B:N shifted to 1.13. By using saturated ALD half cycles, the amount of residual chlorine in the film was reduced to 2.5% after atomic H exposure for the 60 ALD cycles at 350ºC to remove surface Cl. This BN film was estimated to be ~5 nm thick by accounting for the Si 2p signal attenuation and electron escape depth. Due to the

demonstration of saturating half-cycles in Fig. 2.1, a fairly constant growth rate of ~0.08 nm/cycle was estimated. As a result, nearly stoichiometric amorphous BN was formed with low levels of oxygen, carbon, and chlorine incorporation (<5%) on $Si_{0.7}Ge_{0.3}$(001).

To determine film conformality, AFM was conducted on the HF-cleaned and BN deposited surfaces (Fig. 2.3). The HF-cleaned surface (Fig. 2.3(a)) was extremely flat and had a corresponding root mean square (RMS) surface roughness of 0.104 nm for a 1 μm x 1 μm area. The RMS roughness after 60 cycles of BN deposition was still only 0.276 nm; this sub-nanometer roughness and lack of evidence of pinholes was consistent with the ALD BN deposition on $Si_{0.7}Ge_{0.3}$(001) being conformal. To further investigate the quality of the 60 cycles BN film, metal-oxide-semiconductor insulator-capacitors (MOSCAPs) were fabricated by depositing 50 nm of 150 μm Ni dots on the BN layer. Corresponding capacitance-voltage and current-voltage measurements indicated that the film was sufficiently insulating and pinhole free by achieving a capacitance and measuring a leakage of $2.69 * 10^{-4}$ A/cm^2 at a gate bias of -2V after a forming gas anneal. For integration of TMDs on commercial 300 mm Si wafers, or high-hole mobility SiGe films on Si wafers, an insulating ultrathin diffusion barrier is needed *(18, 28)*. This pinhole-free BN layer on $Si_{0.7}Ge_{0.3}$(001) shows the ease of formation of insulating nanoscale BN on commercial wafers.

2.4.2 Cu

As a comparison to the $Si_{0.3}Ge_{0.7}$(001) surface, sequential exposures of N_2H_4 and BCl_3 were performed on Cu on SiO_2/Si. Fig. 2.4 shows the XPS spectra corrected with Schofield values and inelastic mean free paths normalized to Cu 2p. XPS was collected

for the as loaded, UHV annealed, and atomic H cleaned surface, and after BN cycles at 350°C using the saturation conditions determined by the ALD on $Si_{0.3}Ge_{0.7}$(001). From XPS characterization, the final film after 50 ALD cycles had less than 5% oxygen incorporation, negligible carbon, and only 6% Cl. Note, in contrast to the $Si_{0.7}Ge_{0.3}$(001) surface, no surface nitride was present on the Cu 2p peak. Although the substrate Si signal was absent after the 50 ALD cycles, consistent with the Cu layer being intact, AFM studies showed an increase in surface roughness after ALD consistent with slight etching of Cu. The slightly higher amount of Cl for ALD on Cu vs. $Si_{0.7}Ge_{0.3}$(001) can be attributed to using non-optimized dosing conditions for the Cu study.

To study the surface topography, AFM images were taken of the as loaded sample (Fig. 2.5 (a)) after the atomic H clean (b) and after 50 cycles (c). Note the AFM image taken after the atomic H clean required exposing the sample to air and likely surface oxidation. After atomic H cleaning, there was a noticeable change in the surface topology, consistent with Cu grain growth; this phenomena is attributed to a driving force to reduce Cu grain boundary energy *(29)*. Small ~2-4 nm deep holes were also present, attributed to inhomogeneous atomic H etching *(30)*. The RMS roughness of the as loaded surface was 1.259 nm; after the H clean and air exposure, it was 2.886 nm, and after the 50 cycles of BN, it was 7.519 nm. The increase in the RMS roughness was correlated with an increase in Cu grain coarsening, but etching cannot be excluded.

2.4.3 HOPG

BN deposition was studied on HOPG and characterized with in-situ XPS and STM. Fig. 2.6 (a) shows a 50 nm x 50 nm STM image of clean HOPG UHV annealed at

400°C for 1 hour. To check for reactivity on HOPG, large initial exposures of (b) BCl_3 and (c) N_2H_4 were performed. To ensure sufficient exposure, 500 ML BCl_3 was exposed to the HOPG surface; however, virtually no B 1s or Cl 2p counts were detected with XPS, and the corresponding STM image showed only minor bright sites that might have indicated reactivity at defects. Similarly, after several pulses corresponding to 15 ML of N_2H_4 exposure to the clean HOPG surface, the N 1s XPS signal could not be detected; however, in STM, clear 1.7 ± 0.3 nm tall features were present on the surface at the step edges. This is consistent with nucleation by N_2H_4. Since an XPS saturation study could not be executed due to insignificant changes in coverage during half cycle exposures, additional ALD cycles were dosed and characterized with XPS. To further study the growth of BN on these features, 30 cycles of 5 ML BCl_3 + 2 ML N_2H_4 (corresponding to 1 second pulses) were performed. The corresponding STM images presented in Fig. 2.7. show the ALD induced features have a maximum height of ~2.2 nm and a width of ~100-200 nm. In XPS, the films showed ~8% B and 7% N with Cl and O both comprising less than 1% of the film concentration normalized to the area of C 1s after 30 cycles (Fig 2.8). It should be noted that half cycle reactions did not appear to saturate in a traditional ALD sense as shown by STM imaging; when half-cycle exposures of N_2H_4 and BCl_3 became too large (>10ML), evidence of substrate etching near the decorated step edges was observed. Since only 1-2 monolayer of BN would be needed in a practical device, this may not be significant in some applications.

2.5 Discussion and Conclusion

To understand the mechanism of ALD on $Si_{0.3}Ge_{0.7}(001)$, in comparison to the etching witnessed on Cu, it is first necessary to understand the surface chemistry. On $Si_{0.3}Ge_{0.7}(001)$, N_2H_4 was observed to nitridate the surface, forming Si-NH_x bonds, as previously reported *(23)*. By forming a surface with Si-NH_x, subsequent half-cycle dosing with BCl_3 is well suited to form Si-N-BCl_x with an HCl(g) desorption product. This surface nitridation prevents BCl_3 and perhaps any Cl byproducts from reaching the surface and forming Si-Cl_x species, such as volatile $SiCl_4$. On Cu, the driving force to form Cu-NH_x bonds is low since the standard heat of formation of Cu_3N is endothermic *(31)*; hence, no shifted Cu-N component is seen in the Cu 2p XPS spectrum. Due to this poor reactivity, and hence poor passivation, this allows BCl_3 and potential Cl_2 gas to find Cu sites and induce formation of volatile Cu-Cl species, such as Cu_3Cl_3. This tendency for Cu-Cl formation, coupled with non-optimized dosing on Cu, can help explain the larger amount of Cl residue seen in the BN film on Cu in comparison to residues seen in films grown on $Si_{0.3}Ge_{0.7}(001)$ and HOPG surfaces.

After cyclic exposures, the BN grew anisotropically out from the step edges corresponding to 5.0 ± 1.7 nm/cycle in the planar direction compared to only 0.05 ± .01 nm/cycle in the vertical direction based on the average final feature size after 30 cycles of deposition. Due to the etching that was witnessed near the decorated step edges from non-saturating exposures greater than 10 ML, the quantification of growth rate was challenging, and thus the accuracy of these numbers is limited. However, these values support the hypothesis that nitrided HOPG step edges were required to catalyze the reaction leading to the higher growth rate in the planar dimension. This propensity to

grow in the planar direction can further support the pinhole-free film seen on $Si_{0.3}Ge_{0.7}$(001) and the corresponding electrical data.

A novel BN ALD process at 350°C has been accomplished on the $Si_{0.3}Ge_{0.7}$(001) surface using N_2H_4 and BCl_3 with the resulting BN thin film being uniform and pin-hole free. Nearly stoichiometric amorphous BN with low oxygen, carbon, and chlorine incorporation resulted. The sufficiently insulating pinhole-free amorphous BN film could be used for the integration of TMDs on commercial wafers, in which an ultrathin diffusion barrier is needed. On HOPG, the N_2H_4 was reactive to the step edges, and subsequent cycles after the initial decoration displayed the tendency for BN films to grow anisotropically in the planar direction. Therefore, in general, for substrates that can react with N_2H_4 and form a nitride protection layer, amorphous BN should be grown without etching of the substrate when using BCl_3. The resulting films will be oxygen and carbon free, as well as conformal.

2.6 Acknowledgements

This work was performed in part at the San Diego Nanotechnology Infrastructure (SDNI) of UCSD, a member of the National Nanotechnology Coordinated Infrastructure, which is supported by the National Science Foundation (Grant ECCS-1542148) and by SWAN, a funded center of NRI, a Semiconductor Research Corporation (SRC) program sponsored by NERC and NIST. Additionally, the authors would also like to thank Rasirc, Inc and Applied Materials, Inc, for further support, as well as Michael Breeden for the chamber schematic.

Chapter 2, in part or in full, is a reprint of the material as it appears in Applied Surface Science. S. Wolf, M. Edmonds, K. Sardashti, M. Clemons, J. Park, N. Yoshida, L. Dong, R. Holmes, D. Alvarez, and A. Kummel. "Low-Temperature Amorphous Boron Nitride on $Si_{0.7}Ge_{0.3}$(001), Cu, and HOPG from Sequential Exposures of N_2H_4 and BCl_3." *Applied Surface Science*. *(2018)*. The dissertation author was the primary investigator and author of this paper.

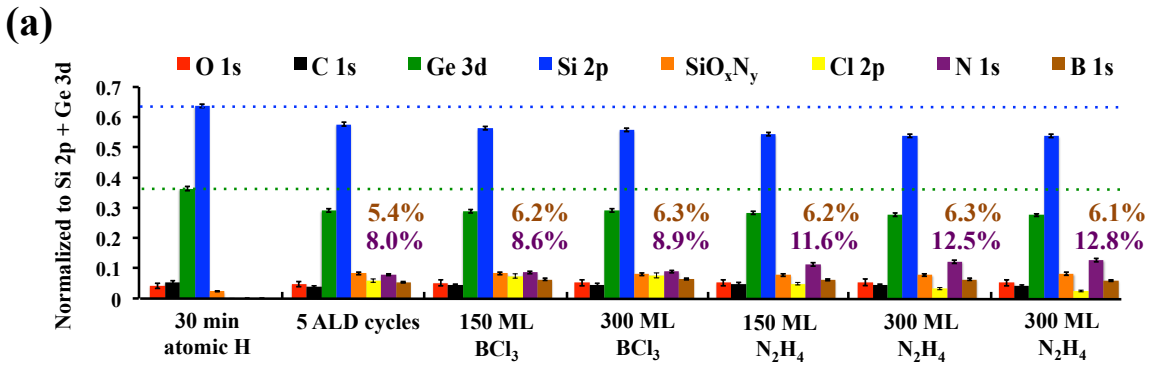

Figure 2.1: Saturation study of BN growth on $Si_{0.7}Ge_{0.3}$(001). Atomic H clean was performed at 330°C, and 5 ALD cycles of 150 ML N_2H_4 and 150 ML BCl_3 exposures were performed at 350°C. The percentage of nitrogen (purple) and boron (brown) are explicitly listed for each experiment. Each exposure is in addition to the previous surface treatment.

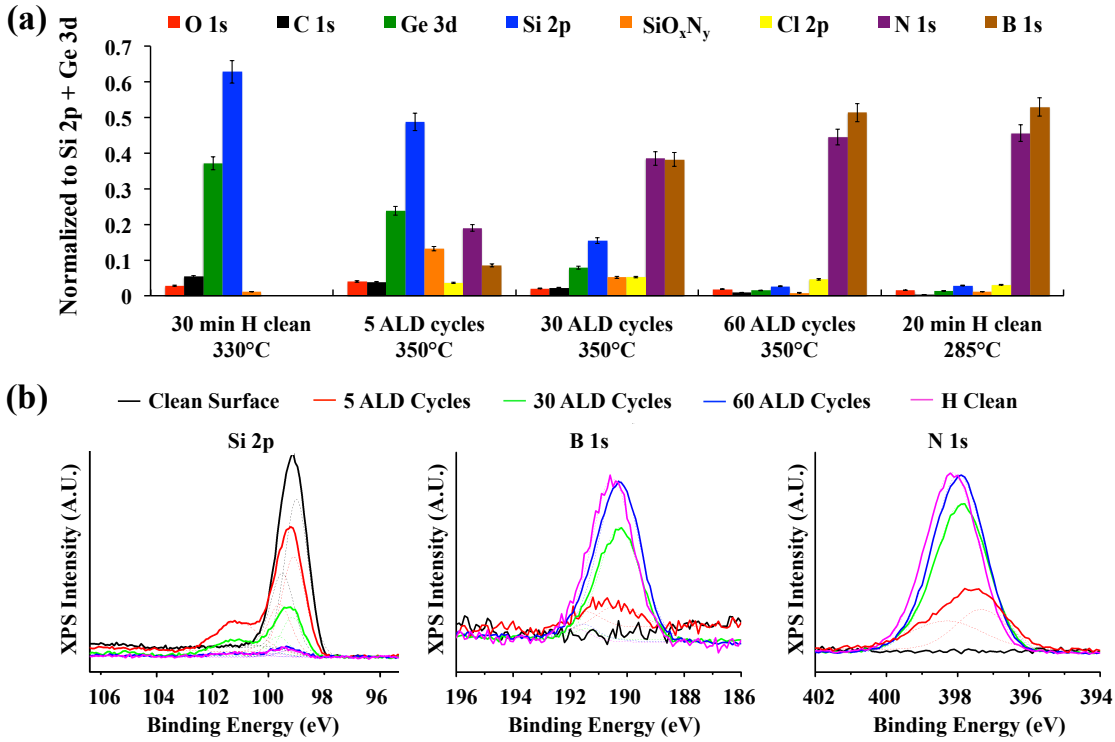

Figure 2.2: XPS of BN Growth on $Si_{0.7}Ge_{0.3}$(001). (a) XPS corrected peak areas normalized to Si 2p + Ge 3d for clean surface, 5 cycles, 30 cycles, and after 60 cycles BN. A final H clean was performed to remove surface Cl. (b) XPS Si 2p, B 1s, and N 1s raw peak areas for the clean surface after 5 cycles, 30 cycles, and 60 cycles. Note the formation of a higher binding energy SiN_x component after 5 ALD cycles.

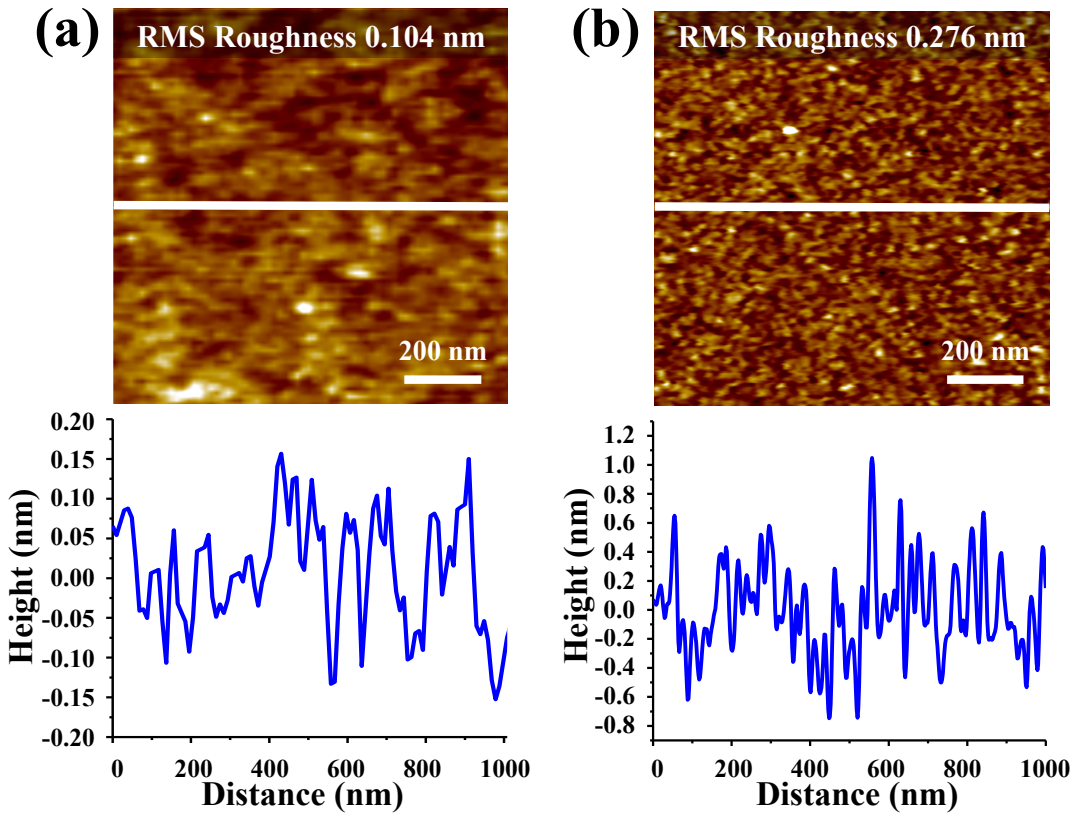

Figure 2.3: AFM of BN growth on $Si_{0.7}Ge_{0.3}$(001). 1μm x 1μm AFM images of (a) HF treated $Si_{0.7}Ge_{0.3}$(001) and (b) 60 cycles BN ALD on $Si_{0.7}Ge_{0.3}$(001).

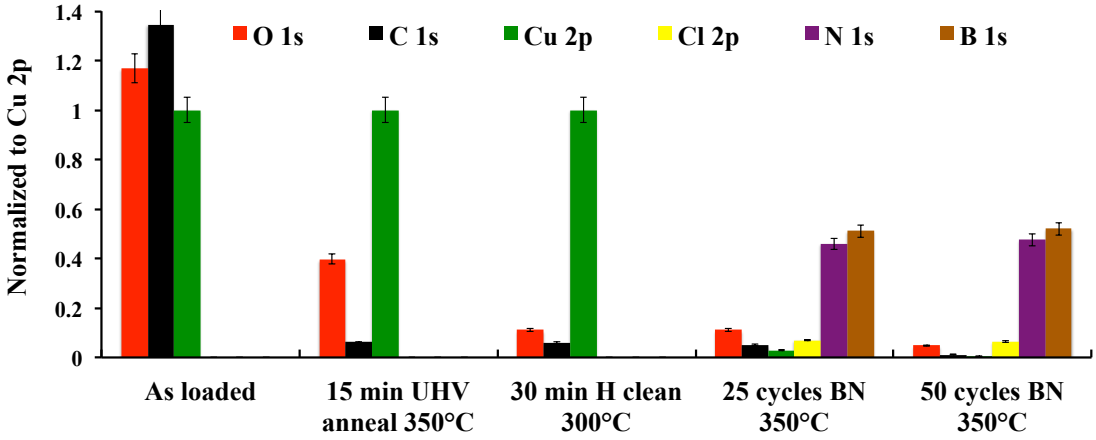

Figure 2.4: BN Growth on Cu. XPS of as loaded, UHV annealed, atomic H cleaned and after 25 and 50 cyclic exposures to N_2H_4 and BCl_3. After 50 cycles, 4.8% oxygen, 6.4% chlorine, and <1% carbon were present in the film.

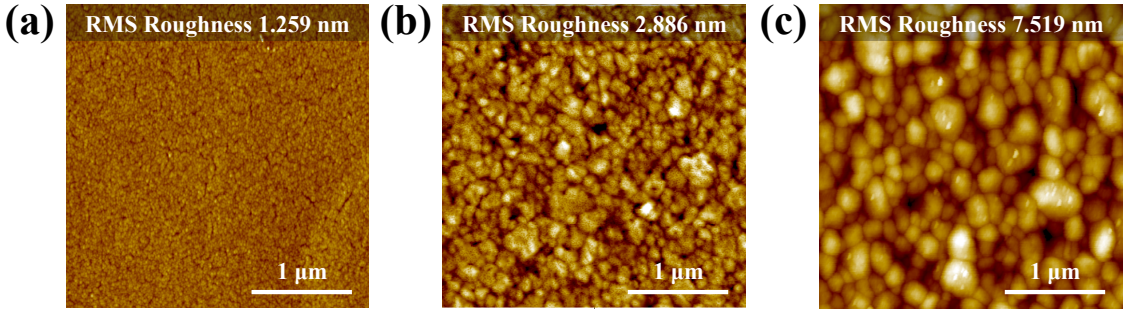

Figure 2.5: AFM of Cu samples. 3 µm x 3 µm AFM images of (a) as loaded Cu, (b) after H clean and air exposure, and (c) after 50 cycles of sequential exposures of N_2H_4 and BCl_3.

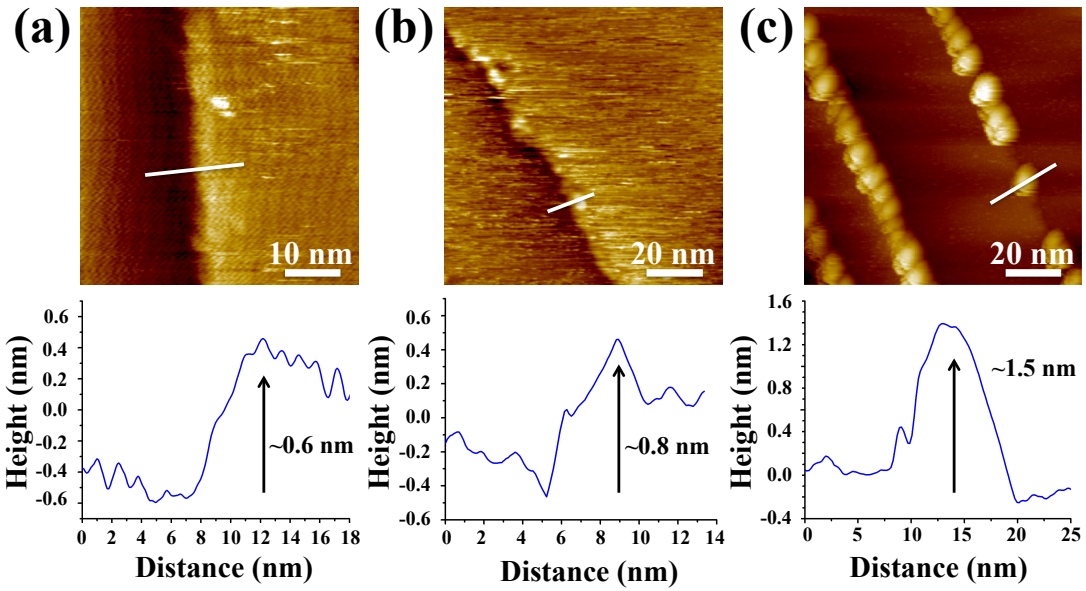

Figure 2.6: *In situ* STM images of HOPG before and after 1 cycle of BCl_3 + N_2H_4. STM images of (a) tape-cleaned HOPG annealed at 400°C for 1 hour, (b) after 500 ML BCl_3 exposure at 350°C, and (c) after 15 ML N_2H_4 exposure at 350°C.

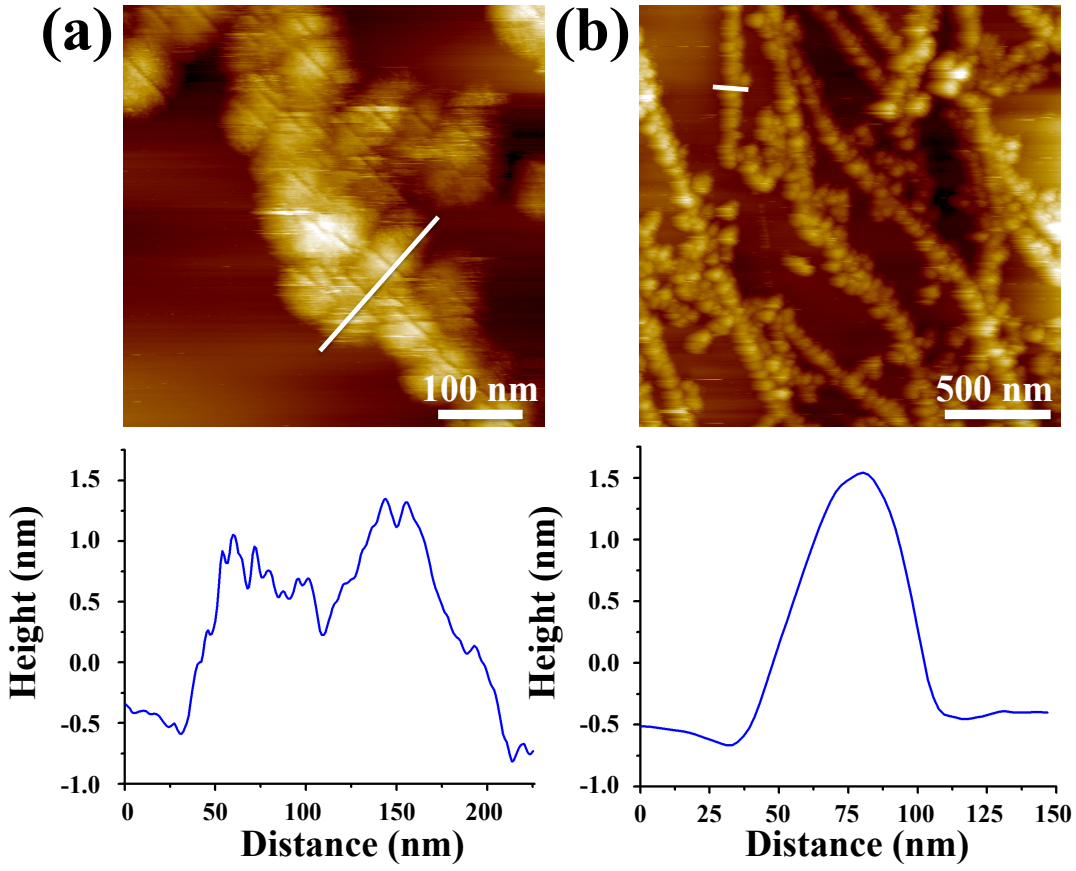

Figure 2.7: *In Situ* STM images of HOPG before and after 30 cycles of BCl_3 + N_2H_4. (a) 500 nm x 500 nm and (b) 2 µm x 2 µm STM images and respective line traces of 30 cycles of 5 ML BCl_3 + 2 ML N_2H_4.

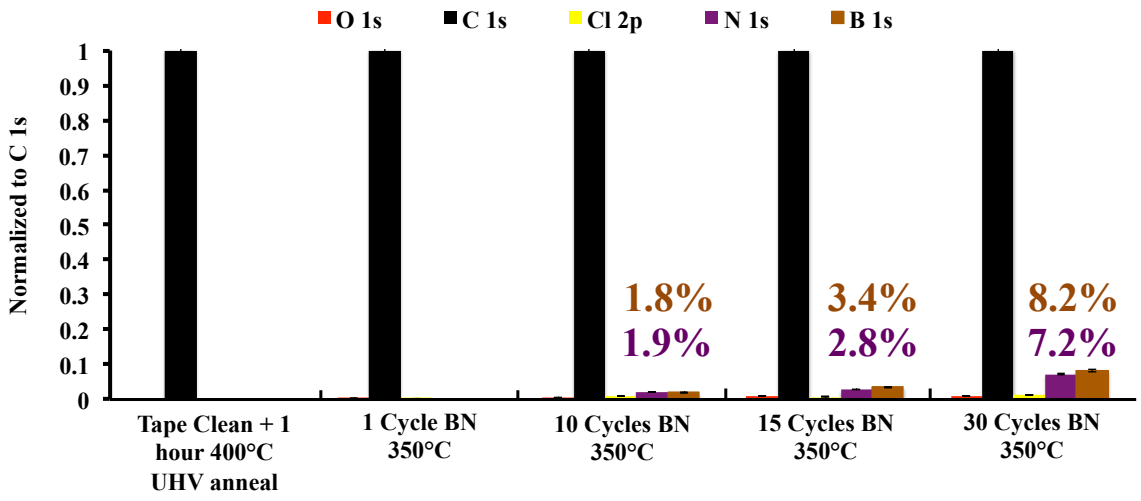

Figure 2.8: XPS of BN growth on HOPG. (a) XPS corrected peak areas normalized to C 1s for the clean HOPG surface followed by BN cycles at 350°C. Only C 1s is detectable through the first cycle of BN. Additional cycles leads to <1% concentrations of O and Cl on the surface.

2.7 References

1. Pierson, H.O., *Handbook of Refractory Carbides & Nitrides: Properties, Characteristics, Processing and Apps*. 1996: William Andrew.

2. Kim, K.K., Hsu, A., Jia, X., Kim, S.M., Shi, Y., Hofmann, M., Nezich, D., Rodriguez-Nieva, J.F., Dresselhaus, M., Palacios, T. and Kong, J, *Synthesis of monolayer hexagonal boron nitride on Cu foil using chemical vapor deposition.* Nano letters, 2011. **12**(1): p. 161-166.

3. Tay, R.Y., Griep, M.H., Mallick, G., Tsang, S.H., Singh, R.S., Tumlin, T., Teo, E.H.T. and Karna, S.P., *Growth of large single-crystalline two-dimensional boron nitride hexagons on electropolished copper.* Nano letters, 2014. **14**(2): p. 839-846.

4. Ferguson, J., A. Weimer, and S. George, *Atomic layer deposition of boron nitride using sequential exposures of BCl 3 and NH 3.* Thin Solid Films, 2002. **413**(1): p. 16-25.

5. Haider, A., Ozgit-Akgun, C., Goldenberg, E., Okyay, A.K. and Biyikli, N., *Low-Temperature Deposition of Hexagonal Boron Nitride via Sequential Injection of Triethylboron and N2/H2 Plasma.* Journal of the American Ceramic Society, 2014. **97**(12): p. 4052-4059.

6. Lipp, A., K.A. Schwetz, and K. Hunold, *Hexagonal boron nitride: fabrication, properties and applications.* Journal of the European Ceramic Society, 1989. **5**(1): p. 3-9.

7. Dean, C.R., Young, A.F., Meric, I., Lee, C., Wang, L., Sorgenfrei, S., Watanabe, K., Taniguchi, T., Kim, P., Shepard, K.L. and Hone, J., *Boron nitride substrates for high-quality graphene electronics.* Nature nanotechnology, 2010. **5**(10): p. 722-726.

8. Bath, A., Van Der Put, P.J., Becht, J.G.M., Schoonman, J. and Lepley, B., *Plasma enhanced chemical vapor deposition and characterization of boron nitride gate insulators on InP.* Journal of Applied Physics, 1991. **70**(8): p. 4366-4370.

9. Nguyen, S.V., Nguyen, T., Treichel, H. and Spindler, O., *Plasma-Assisted Chemical Vapor Deposition and Characterization of Boron Nitride Films.* Journal of The Electrochemical Society, 1994. **141**(6): p. 1633-1638.

10. King, S.W., French, M., Bielefeld, J., Jaehnig, M., Kuhn, M. and French, B., *X-ray photoelectron spectroscopy investigation of the Schottky barrier at a-BN: H/Cu interfaces.* Electrochemical and Solid-State Letters, 2011. **14**(12): p. H478-H479.

11. Britnell, L., Gorbachev, R.V., Jalil, R., Belle, B.D., Schedin, F., Mishchenko, A., Georgiou, T., Katsnelson, M.I., Eaves, L., Morozov, S.V. and Peres, N.M.R., *Field-effect tunneling transistor based on vertical graphene heterostructures.* Science, 2012. **335**(6071): p. 947-950.

12. Snure, M., Paduano, Q., Hamilton, M., Shoaf, J. and Mann, J.M., *Optical characterization of nanocrystalline boron nitride thin films grown by atomic layer deposition.* Thin Solid Films, 2014. **571, Part 1**: p. 51-55.

13. Olander, J., Ottosson, L.M., Heszler, P., Carlsson, J.O. and Larsson, K.M., *Laser-Assisted Atomic Layer Deposition of Boron Nitride Thin Films.* Chemical Vapor Deposition, 2005. **11**(6-7): p. 330-337.

14. Ci, L., Song, L., Jin, C., Jariwala, D., Wu, D., Li, Y., Srivastava, A., Wang, Z.F., Storr, K., Balicas, L. and Liu, F., *Atomic layers of hybridized boron nitride and graphene domains.* Nature materials, 2010. **9**(5): p. 430-435.

15. Song, L., Ci, L., Lu, H., Sorokin, P.B., Jin, C., Ni, J., Kvashnin, A.G., Kvashnin, D.G., Lou, J., Yakobson, B.I. and Ajayan, P.M., *Large scale growth and characterization of atomic hexagonal boron nitride layers.* Nano letters, 2010. **10**(8): p. 3209-3215.

16. Liu, Z., Song, L., Zhao, S., Huang, J., Ma, L., Zhang, J., Lou, J. and Ajayan, P.M., *Direct growth of graphene/hexagonal boron nitride stacked layers.* Nano letters, 2011. **11**(5): p. 2032-2037.

17. Hemmi, A., Bernard, C., Cun, H., Roth, S., Klöckner, M., Kälin, T., Weinl, M., Gsell, S., Schreck, M., Osterwalder, J. and Greber, T., *High quality single atomic layer deposition of hexagonal boron nitride on single crystalline Rh (111) four-inch wafers.* Review of Scientific Instruments, 2014. **85**(3): p. 035101.

18. Chen, M.C., Lin, C.Y., Li, K.H., Li, L.J., Chen, C.H., Chuang, C.H., Lee, M.D., Chen, Y.J., Hou, Y.F., Lin, C.H. and Chen, C.C., *Hybrid Si/TMD 2D electronic double channels fabricated using solid CVD few-layer-MoS2 stacking for V th matching and CMOS-compatible 3DFETs*. in *Electron Devices Meeting (IEDM), 2014 IEEE International*. 2014. IEEE.

19. Wang, L., Jie, J., Shao, Z., Zhang, Q., Zhang, X., Wang, Y., Sun, Z. and Lee, S.T., *MoS2/Si Heterojunction with Vertically Standing Layered Structure for Ultrafast, High-Detectivity, Self-Driven Visible–Near Infrared Photodetectors.* Advanced Functional Materials, 2015. **25**(19): p. 2910-2919.

20. Kaloyeros, A. and E. Eisenbraun, *Ultrathin diffusion barriers/liners for gigascale copper metallization.* Annual review of materials science, 2000. **30**(1): p. 363-385.

21. Braud, F., Torres, J., Palleeau, J., Mermet, J.L., Marcadal, C. and Richard, E., *Ultra thin diffusion barriers for Cu interconnections at the gigabit generation and beyond.* Microelectronic engineering, 1997. **33**(1-4): p. 293-300.

22. Lemme, M.C., Echtermeyer, T.J., Baus, M. and Kurz, H., *A graphene field-effect device.* IEEE Electron Device Letters, 2007. **28**(4): p. 282-284.

23. Edmonds, M., Sardashti, K., Wolf, S., Chagarov, E., Clemons, M., Kent, T., Park, J.H., Tang, K., McIntyre, P.C., Yoshida, N. and Dong, L., *Low temperature thermal ALD of a SiNx interfacial diffusion barrier and interface passivation layer on SixGe1− x (001) and SixGe1− x (110).* The Journal of Chemical Physics, 2017. **146**(5): p. 052820.

24. Burke, M., Blake, A., Povey, I.M., Schmidt, M., Petkov, N., Carolan, P. and Quinn, A.J., *Low sheet resistance titanium nitride films by low-temperature plasma-enhanced atomic layer deposition using design of experiments methodology.* Journal of Vacuum Science & Technology A: Vacuum, Surfaces, and Films, 2014. **32**(3): p. 031506.

25. Musschoot, J., Xie, Q., Deduytsche, D., Van den Berghe, S., Van Meirhaeghe, R.L. and Detavernier, C., *Atomic layer deposition of titanium nitride from TDMAT precursor.* Microelectronic Engineering, 2009. **86**(1): p. 72-77.

26. Hendrickson, D.N., J.M. Hollander, and W.L. Jolly, *Core-electron binding energies for compounds of boron, carbon, and chromium.* Inorganic Chemistry, 1970. **9**(3): p. 612-615.

27. Trehan, R., Y. Lifshitz, and J. Rabalais, *Auger and x‐ray electron spectroscopy studies of h BN, c BN, and N+ 2 ion irradiation of boron and boron nitride.* Journal of Vacuum Science & Technology A: Vacuum, Surfaces, and Films, 1990. **8**(6): p. 4026-4032.

28. Liu, Y.J., Hao, L.Z., Gao, W., Liu, Y.M., Li, G.X., Xue, Q.Z., Guo, W.Y., Yu, L.Q., Wu, Z.P., Liu, X.H. and Zeng, H.Z., *Growth and humidity-dependent electrical properties of bulk-like MoS 2 thin films on Si.* RSC Advances, 2015. **5**(91): p. 74329-74335.

29. Du, S. and Y. Li, *Effect of annealing on microstructure and mechanical properties of magnetron sputtered Cu thin films.* Advances in Materials Science and Engineering, 2015. **2015**.

30. Wu, F., G. Levitin, and D.W. Hess, *Low-temperature etching of Cu by hydrogen-based plasmas.* ACS Applied Materials & Interfaces, 2010. **2**(8): p. 2175-2179.

31. Gale, W.F. and T.C. Totemeier, *Smithells metals reference book*. 2003: Butterworth-Heinemann.

Chapter 3

Low Temperature Thermal ALD TaN_x and TiN_x Films from Anhydrous N_2H_4

3.1 Abstract

Thermal ALD of TaN_x and TiN_x films was performed using hydrazine (N_2H_4) as a reactive N-containing source. Ultralow temperature (100ºC and 300ºC) growth of TaN_x was observed using N_2H_4 and tris(diethylamido)(tert-butylimido) tantalum (TBTDET); XPS showed nearly stoichiometric Ta_3N_5 films were deposited with below 10% O and 5% C incorporation. Stoichiometric TiN_x films grown at 300ºC with tetrakis(dimethylamido) titanium (TDMAT) showed an RMS roughness below 2 nm consistent with good nucleation density. High conductivity nitride films were grown by a thermal low-temperature TiN_x ALD process using anhydrous N_2H_4 and titanium tetrachloride ($TiCl_4$) from 300-400ºC; uniform, nearly stoichiometric films of 0.44 nm RMS roughness were deposited. Compared to NH_3 grown films, XPS confirmed N_2H_4 grown films contained fewer O, C, and Cl impurities consistent with lower resistivities being observed with N_2H_4. The data is consistent with N_2H_4 serving as a reducing agent and a good proton donor to Ta and Ti ligands.

3.2 Introduction

Deposition of ultra-thin barrier layers on high aspect ratio features is a crucial processing component in microelectronic devices. As such, the need to deposit precise conformal barrier layers with thickness and stoichiometry control via an atomic layer deposition process is required. Two such barrier layers, titanium nitride (TiN) and

tantalum nitride (TaN) have been extensively studied in devices because of their ideal thermal, mechanical, and electrical properties and ability to act as metal diffusion barriers (*1-4*). In particular, TiN has been shown to act as an efficient diffusion barrier to WF_6 during W metal fill (*3*). Similarly, tantalum nitride (TaN) has been utilized as a diffusion barrier to Cu on low-k insulators, such as SiO_2 or SiOCH, as Cu can readily diffuse into insulators lowering device reliability (*5, 6*). ALD TiN and TaN films have previously been performed using a wide range of precursors including halides (i.e. TiI_4, $TiCl_4$, $TaCl_5$, TaF_5) (*1, 7-9*) and metal organics (i.e. TDMAT, TEMAT, TBTDET) (*6, 10-14*), as well as nitrogen sources (thermal/plasma NH_3, N_2/H_2, etc). Metal halide precursors are typically preferred over organometallic grown films to lower impurities when there is no concern about metal corrosion, such as in capping HfO_2 (*15*) or for TiN/HfO_2 gate stacks (*16*). In comparison, organometallic-grown films usually contain higher levels of residual carbon and oxygen contamination, which has been correlated with an increase in film resistivity (*13, 14*). Commercial processing on 200 and 300 mm wafers showed that $TiCl_4$ + NH_3 at 400ºC achieved low resistivities for films approximately >20 nm (*17*), but plasma enhanced-ALD TiN was needed achieve optimal growth rates with lower contamination at temperatures near 350°C; however, the film and underlying substrate can suffer from plasma-induced damage (*1, 18*).

For the results presented in this work, low-temperature thermal deposition of TaN and TiN films using sequential exposures of anhydrous N_2H_4 (*19*) and either TBTDET, TDMAT, or $TiCl_4$ were performed. Insulating SiO_2/Si substrates were utilized in order to perform electrical characterization of deposited films. Since anhydrous N_2H_4 was used as the reactive nitrogen source, the barrier for surface reactions to occur with each precursor

can be reduced compared to using thermal NH_3; the dissociation of N_2H_4 through the breaking of a N-N bond is more energetically favorable than having to dissociate a more tightly bound N-H bond in NH_3. The N-N single bond in N_2H_4 has an energy of ~3 eV, while the N-H single bond in NH_3 has an energy of ~4.5 eV (*20*). Moreover, the purity of the N_2H_4 allows for deposition of films without uptake of oxygen or carbon contamination, which has previously been demonstrated with SiN_x (*21*) and BN (*22*) films. A novel metal halide TiN_x ALD process was developed with $TiCl_4$ and N_2H_4 that produced resistivities of 593 μohm-cm and 359 μohm-cm at 300ºC and 400ºC, respectively that could readily be incorporated into MOS gate stack architectures. Note, this is the first time ALD titanium nitride has been reported in the literature with $TiCl_4$ and N_2H_4.

3.3 Experimental

The substrates used in this study consisted of 300 nm of thermal SiO_2 grown on Si(001) (University Wafer). Samples underwent an *ex situ* degrease involving quick rinses in acetone, methanol, and water before being loaded into the vacuum chamber. Once loaded into the UHV chamber, the samples were heated to 350°C for 30 minutes to remove any physisorbed surface contamination. Precursor exposures were performed in a deposition chamber, which has been described in detail elsewhere (*22*). The deposition chamber and dosing lines were pumped with a turbomolecular pump, but the actual deposition was performed through only a backing pump with a base pressure of ~$1x10^{-2}$ Torr. The chamber was heated ~100°C, and dosing lines were kept ~10-20ºC warmer to ensure precursors would not condense on the chamber walls. In addition, the N_2H_4 vessel

was pressurized to ~750 torr with ultrahigh purity N_2 that was passed through a purifier to act as a push gas for the N_2H_4. NH_3 from Praxair with a purity of 99.9% was used for TiN_x experiments undiluted. Precursor exposures are presented in MegaLangmuirs (MegaLs where 1 MegaL = 1 Torr for 1 sec), and were calculated from exposure time and pressure of the precursor; however, it should be noted that the values presented for exposures of N_2H_4 do not account for the dilution with N_2. As an estimation, by using the vapor pressure of N_2H_4 at room temperature, the amount of N_2H_4 was likely ~1-2% of the total exposure. Before moving samples into the deposition chamber, samples were preheated in the UHV chamber. In both chambers, samples were radiatively heated by a pyrolytic boron nitride heater. After exposure to anhydrous N_2H_4 (Rasirc) and either $TiCl_4$ (Strem Chemicals), TDMAT (Sigma-Aldrich), or TBTDET (Sigma-Aldrich) samples were transferred back to the UHV chamber where *in situ* x-ray photoelectron spectroscopy (XPS) was performed without breaking vacuum. A monochromatic XPS system (Al kα hν = 1486.7 eV) was used to collect surface-sensitive spectra at an angle of 60° with respect to the surface normal. Additionally, an electron pass energy of 50 eV and a line width of 0.1 eV were used. XPS spectra analysis was conducted with CASA XPS v.2.3 utilizing Shirley background subtractions. Schofield photoionization cross sectional relative sensitivity factors were used to correct raw peak areas before normalization. In addition to XPS, surface topography was characterized with atomic force microscopy (AFM). Lastly, the resistance of air-exposed thin films was measured using a modified four-point probe measurement, in which 30 nm thick Ni dots with 150 μm diameters and 250 μm spacing were deposited on top of ALD TiN_x and TaN_x films. Resistivities were approximated by estimating the thickness of deposited films from

cross-sectional scanning electron microscopy (SEM) images. Note the resistivities were measured after air exposure so the actual TiN_x thicknesses are probably less than those measured by SEM since the top few nanometers may have been oxidized and converted to high resistivity TiO_xN_y (*23*).

3.4 TaN_x from TBTDET

Anhydrous N_2H_4 chemistry was applied to ALD at very low temperatures with an organometallic Ta precursor (TBTDET); saturation data documenting the ALD deposition at 150ºC is shown in Fig. 3.1. Higher sample temperature saturation was not tested because the uniformly high valance of the Ta in the film showed the N_2H_4 did not have the ability to reduce the Ta in the TDTBET; instead the data was consistent with the need for a lower valent Ta precursor for reaction with N_2H_4 to form conductive TaN. As shown in Fig. 3.2, AFM imaging indicated a pinhole-free surface with a low RMS surface roughness of 0.25 nm from 15 cyclic exposures of TBTDET and N_2H_4 at 150ºC. Fig. 3.3 shows the XPS of TaN_x films at temperatures between 100ºC and 300ºC. In Fig. 3.3 (a), XPS normalization shows that the films contain nearly 40% C at 100ºC and almost 30% at 300ºC; however, the amount of O is undetectable at 100ºC and only ~4% at higher temperature. Fig. 3.3 (b) shows the raw Ta 4d peak that confirmed the nucleation with TBTDET (Si-O-Ta formation) based on the Ta 4d peak position of ~231eV (*24, 25*). After ALD cycles of TBTDET + N_2H_4, there was an ~ 2eV chemical shift toward lower binding energy consistent with formation of Ta-N bonds in the film. It is noted that the ratio of Ta to N in the deposited films becomes more Ta rich at increasing deposition temperatures. This effect is observed more clearly when looking at

the Ta $4p_{3/2}$ / N 1s region; at higher temperature the N peak shifts to lower BE and becomes more narrow while the Ta component increases in intensity (Fig. 3.3 (d)). In Fig. 3.3 (c), a dose of atomic H at 250ºC was performed on the 150ºC grown film; the C is significantly reduced to ~1.5%. This result was consistent with the C simply accumulating on the top of the film during deposition. The changing Ta/N ratio before and after the 250ºC atomic H exposure in the normalized XPS is most consistent with annealing in the presence of atomic H inducing desorption of a $C_xN_yH_z$ species from the surface (as seen in Figs. 3.3 and 3.4).

Fig. 3.4 shows the XPS Ta $4p_{3/2}$ / N 1s region for a series of experiments in which the clean surface underwent a total of 100 ALD cycles at a deposition temperature of 100ºC followed by UHV anneals up to 250ºC. During the ALD dosing, there was a broad N 1s component located at a BE of ~399 eV along with a very weak Ta $4p_{3/2}$ signal at ~404 eV. Upon annealing, the Ta $4p_{3/2}$ component becomes stronger, and the N 1s peak narrows and shifts toward lower BE. This observed change in the N 1s peak is consistent with the loss of surface CH_xN_y surface species and consistent with the formation of partially crystalline Ta_3N_5 as previously reported in the literature (*26*). When trying to determine the precise oxidation state of the Ta to ascertain if the film is more like conductive TaN (*27*) or insulating Ta_3N_5 (*7*), it is not sufficient to just analyze the Ta 4p region; further evidence of Ta being in an oxidation state higher than +3 can be seen when looking at the peak position of the Ta 4f. From the literature, this corresponds much closer to an average oxidation state of at least Ta^{+4} (*26*). Lastly, resistance measurements were performed on several TaN_x samples; measurements indicated highly resistive films consistent with higher oxidation state Ta TaN_x films. Previous work studying TaN_x

deposition with these precursors similarly resulted in higher than expected resistivity values due to an inability to deposit Ta rich films (*10*).

3.5 TiN_x ALD

3.5.1 TDMAT

In addition to growing films with $TiCl_4$, TiN_x deposition with N_2H_4 and TDMAT was performed. TDMAT grown films are useful for backend processing where using metal-halide precursors, such as $TiCl_4$, are prohibited due to issues of metal corrosion. Fig 3.5. (a) depicts the XPS chemical composition of 100 cycles TDMAT grown films at 300ºC utilizing a 5 second pump after TDMAT exposure and before the following N_2H_4 half cycle. This short pump out time of TDMAT allowed for lower oxygen at ~5% compared to longer pump times where background oxygen and water can incorporate into the film. Fig. 3.5 (b) shows the AFM image and corresponding line trace of the deposited film at 300ºC. The RMS surface roughness was 1.73 nm, about 4x higher than the $TiCl_4$ process (see below), which is likely due to the significant C accumulation on the surface. Fig. 3.5 (c) plots the Ti 2p raw peaks as a function of the TDMAT pump time. It can be seen that for longer pump cycles, the Ti 2p peak position is shifted toward higher BE. This is consistent with background oxygen and/or water reacting with the film before the incoming N_2H_4 completely passivates the surface. Resistance measurements were performed on several deposited TDMAT grown films; the 5 second pump cycle sample had the lowest resistance, ~3,840 ohms (Fig. 3.5 (d)). In SEM, the sample showed a thickness of nearly 50 nm, which places the estimate for resistivity at ~87,000 μohm-cm.

3.5.2 $TiCl_4$

Fig. 3.6 shows the XPS results from saturation dosing that was performed on SiO_2/Si at 300ºC. After undergoing a UHV anneal at 350ºC, the first 1x exposure of 10 MegaL $TiCl_4$ was dosed and reacted on the surface, evidenced by the 0.5% Ti and 2.2% Cl observed in XPS. Subsequently, an additional 2x exposure of 20 MegaL $TiCl_4$ saturated the Ti at 0.6% and Cl at 2.4%. In a similar manner, N_2H_4 saturation dosing was performed using subsequent exposures to a 1x, 2x, and 3x dose where a 1x exposure equals 15 MegaL of N_2H_4 diluted in N_2. After the final 3x dose, the Cl dropped from 2.4% to 1.4%, and the N saturated at 0.8%. This evidence of saturating half-cycle dosing is consistent with a low-temperature thermal ALD procedure utilizing 10 MegaL $TiCl_4$ + 45 MegaL N_2H_4. It should be noted that these large saturation exposures determined from the growth initiation may differ from the amounts needed for steady state deposition. However, during steady state dosing, the density of reactive sites is likely higher than the starting SiO_2 surface providing sufficient confidence that saturated dosing was performed throughout all cycles. This was confirmed by XPS measurements showing that substrate peaks continuously diminished with the number of cycles in a manner consistent with a constant growth rate per cycle.

Once the required pulse size of each half-cycle was determined from the saturation study, thicker films of TiN_x were grown using the saturated recipe of 10 MegaL $TiCl_4$ and 45 MegaL N_2H_4. Fig. 3.7 (a) shows the corrected and normalized XPS of 40 cycles TiN_x at 300ºC. The composition of the 40 cycles film indicated that there was ~20% residual Cl that could be left in the film or on top of the film as a Cl accumulation layer; however, the chemical shift data for Ti in Fig. 3.7 (b) showed only a

small Ti-Cl component in the bulk of the film, consistent with the residual Cl mainly being a surface layer. The level of attenuation of the Si 2p substrate is consistent with 40 cycles being ~5 nm thick.

Fig. 3.7 (b) shows the raw Ti $2p_{3/2}$ and $2p_{1/2}$ spin orbit peaks. A lower binding energy (BE) component located at ~455 eV was consistent with Ti-N bonds, as previously reported in the literature (*28, 29*); it is also known that stoichiometric TiO_2 has a BE near 458-459 eV (*30, 31*). Additionally, since, the deposited film also contains Cl residue, Cl bonds cannot be neglected, and Ti-Cl bonds are known to have a Ti $2p_{3/2}$ BE of ~458.5 eV as well (*32, 33*). Therefore, the component that is located at ~456.5 eV is consistent with a higher N content TiN_x (likely Ti_3N_4) or a substoichiometric TiO_x (*34*). However, as shown in Table 3.1, the high conductivity of the films is consistent with only trace TiO_x in the bulk of the film. It should be noted that precise fitting of the Ti 2p peak was difficult due to the numerous Ti chemical states, as well as the wide range of XPS BE values reported in the literature for TiN, TiN_x, and TiO_xN_y films (*31*). Therefore, for definitive documentation of deposition of TiN, resistivity measurements are required.

In order to perform four-point probe measurements to check the resistivity of deposited films, TiN_x films must be exposed to ambient air conditions for ~1 hour. To quantify the effect of the air exposure, XPS was performed after 1 minute, 5 minutes and 60 minutes of ambient exposure. Fig. 3.8 displays the Ti 2p peak as a function of air exposure times. Along with increasing the amount of surface oxygen and carbon, the oxidation state of the Ti underwent a significant shift. Before ambient exposure, the maximum of the Ti 2p 3/2 peak appeared at 456 eV with a strong TiN component at 455 eV; however, even after just 1 minute of air exposure, O attacked the TiN_x film, evidenced by observing an

~1.5 eV BE shift of the Ti 2p 3/2 peak. After 60 minutes of air exposure, the maximum peak position shifted by about 2 eV, as well as a significant decrease in the TiN component at ~455eV. Additionally, this oxidation could increase the film thickness that was determined with SEM. Both of these effects would be expected to lead to increases in the reported resisitivites in this manuscript, as compared to hypothetical resistivity measurements *in situ.*

To characterize the surface topography, AFM was performed on the 40 cycles of ALD TiN_x film. Fig. 3.9 (a) depicts the bare *ex situ* cleaned surface and (b) after deposition. AFM imaging along with corresponding line traces show the pinhole-free AFM image of 40 cycles of TiN_x at 300ºC compared with the bare SiO_2 surface. Additionally, the deposition was uniform as evidenced by maintaining a low RMS surface roughness of 0.44 nm.

To study the efficacy of N_2H_4 as a TiN precursor, thermal NH_3 was used for comparison. Fig. 3.10 shows the comparison of TiN_x films grown at 400ºC with (a) NH_3 and (b) N_2H_4; there was approximately 2x more O and C and 50% more Cl in 400ºC NH_3 grown films. The source of this increased O incorporation when using NH_3 could arise from side reactions with H_2O/O_2 that can occur from incomplete reaction with NH_3. The higher reactivity of N_2H_4 may rapidly cover the surface with NH_x ligands thereby reducing contamination from background H_2O/O_2. Fig. 3.10 (c) and (d) show the corresponding resistances measured for NH_3 and N_2H_4 grown films, respectively. It should be noted that the ratio of Ti/N for NH_3 grown films is >1, while for N_2H_4 grown films it is <1; however, the amount of O,C, and Cl impurity incorporation prevents the NH_3 grown film from becoming more N-rich, and correspondingly, more conductive.

Table 3.1 summarizes the results of TiN_x films utilizing $TiCl_4$ and either N_2H_4 or NH_3. N_2H_4 films showed lower resistivities, attributed to lower contamination and likely better nucleation density. The best result of 400ºC N_2H_4 showed the lowest residual Cl at 8.7%, which correlated with being the lowest resistivity film estimated at 359 μohm-cm. From the air exposure XPS study, approximately the top 2 nm of the TiN_x films were converted to TiO_xN_y / surface contamination; thus the thickness of TiN_x may be as low as 9 nm so the intrinsic resistivity could equate to as low as 294 μohm-cm for the 400ºC N_2H_4 film.

3.6 Discussion and Conclusion

The anhydrous N_2H_4 chemistry was used with organometallic precursors, TBTDET and TDMAT. For both precursors, thermal processing could not remove all the impurities from the film. For TBTDET, the films deposited were N-rich at low temperature, but became more stoichiometric at higher temperature. Even though after an atomic H exposure was able to reduce the level of C impurity, the TaN_x films displayed insulating behavior. For TDMAT grown films, the oxidation state of the Ti (from the Ti $2p_{3/2}$ component) was more oxidized than the Ti from the $TiCl_4$ process. In the literature, it is well known that atomic H from plasma is required to help reduce the metal, typically through the formation of a more conductive carbide phase (*35, 36*). In order to achieve more conducting films with organometallic precursors from non-plasma processing, lower valence Ti and Ta precursors need to be developed and tested. It is expected that lower valence precursors reacted with N_2H_4 would produce more conductive films.

Thermal low-temperature TiN_x ALD cycles using anhydrous N_2H_4 and $TiCl_4$ were performed at 300-400ºC, and subsequently, conformal, nearly stoichiometric films were deposited as seen in XPS and AFM. Compared to NH_3 grown films, N_2H_4 grown films at both 300ºC or 400ºC showed lower resistivities with fewer impurities. Reported resistivities are likely higher due to significant oxidation of the ultra-thin films, but are still near the best values reported in the literature values for ALD TiN_x films (*14, 37*). In particular, the authors believe the 300ºC thermal N_2H_4 grown TiN_x film with a resisitivity of 593 μohm-cm to be the lowest resistivity film reported for this temperature and thickness.

3.7 Acknowledgements

The authors gratefully acknowledge the support of both Rasirc and Applied Materials. The authors thank Russell Holmes of Rasirc for his assistance with the setup and delivery of pure N_2H_4.

Chapter 3, in part or in full, is reprinted with permission from S. Wolf, M. Breeden, I. Kwak, J. H. Park, M. Kavrik, M. Naik, D. Alvarez, J. Spiegelman, and A. Kummel. "Low-Temperature Thermal ALD TaN_x and TiN_x from Anhydrous N_2H_4." *Applied Surface Science*. *(2018)*. The dissertation author was the primary investigator and author of this paper.

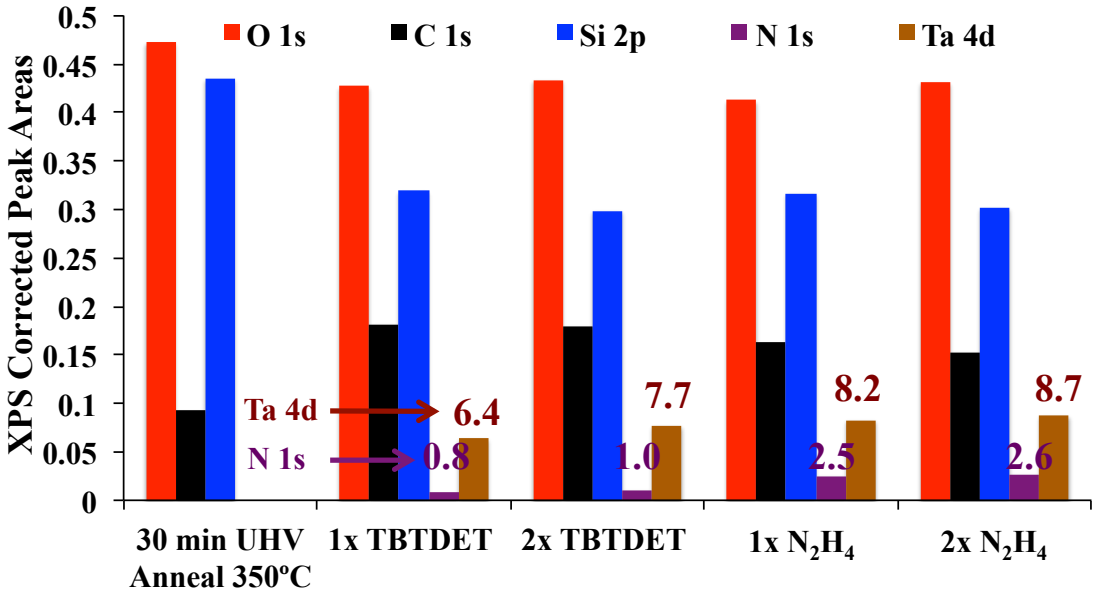

Figure 3.1: XPS Saturation Study of TBTDET and N_2H_4 on Degreased SiO_2/Si at 150ºC. Initial 1x (3 MegaL) TBTDET dose deposited 6.4% Ta on UHV annealed SiO_2/Si. Additional 2x (6 MegaL) TBTDET saturated Ta at 8.0%, while depositing 1.0% N. Similarly, a 1x (15 MegaL) and a 2x (30 MegaL) dose of N_2H_4 were performed, which saturated the N at 2.6%. Self-limiting exposures were consistent with ALD. The TBTDET bottle was heated to ~80°C and utilized an N_2 carrier gas to help deliver TBTDET to the sample.

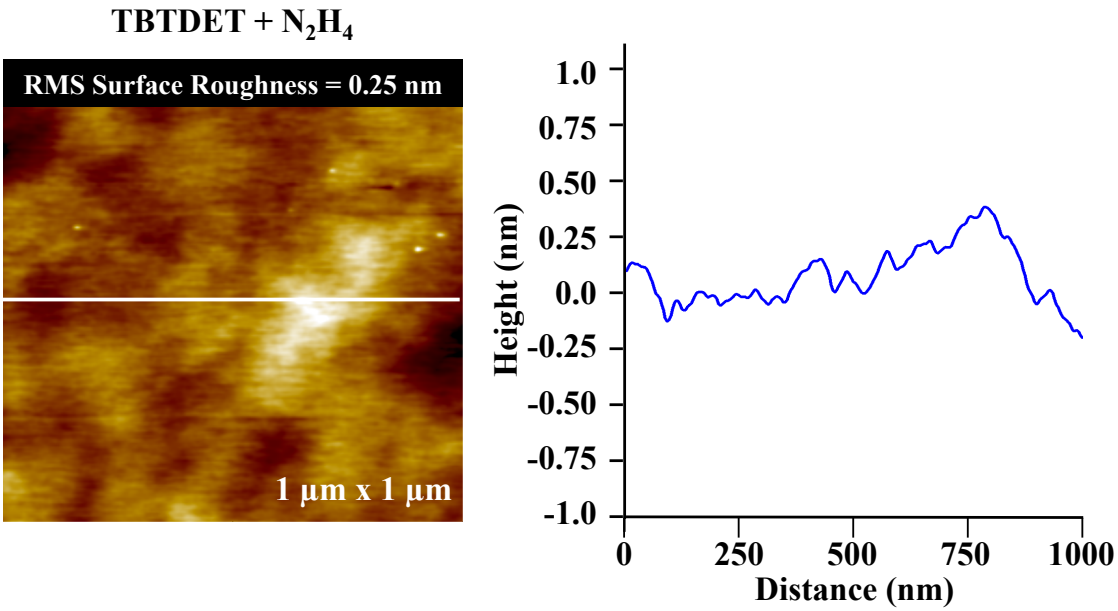

Figure 3.2: *Ex Situ* AFM Imaging. 15 cycles of TaN_x at 150ºC from TBTDET + N_2H_4. The deposited film showed a very low RMS surface roughness of 0.25 nm and no evidence of pinholes.

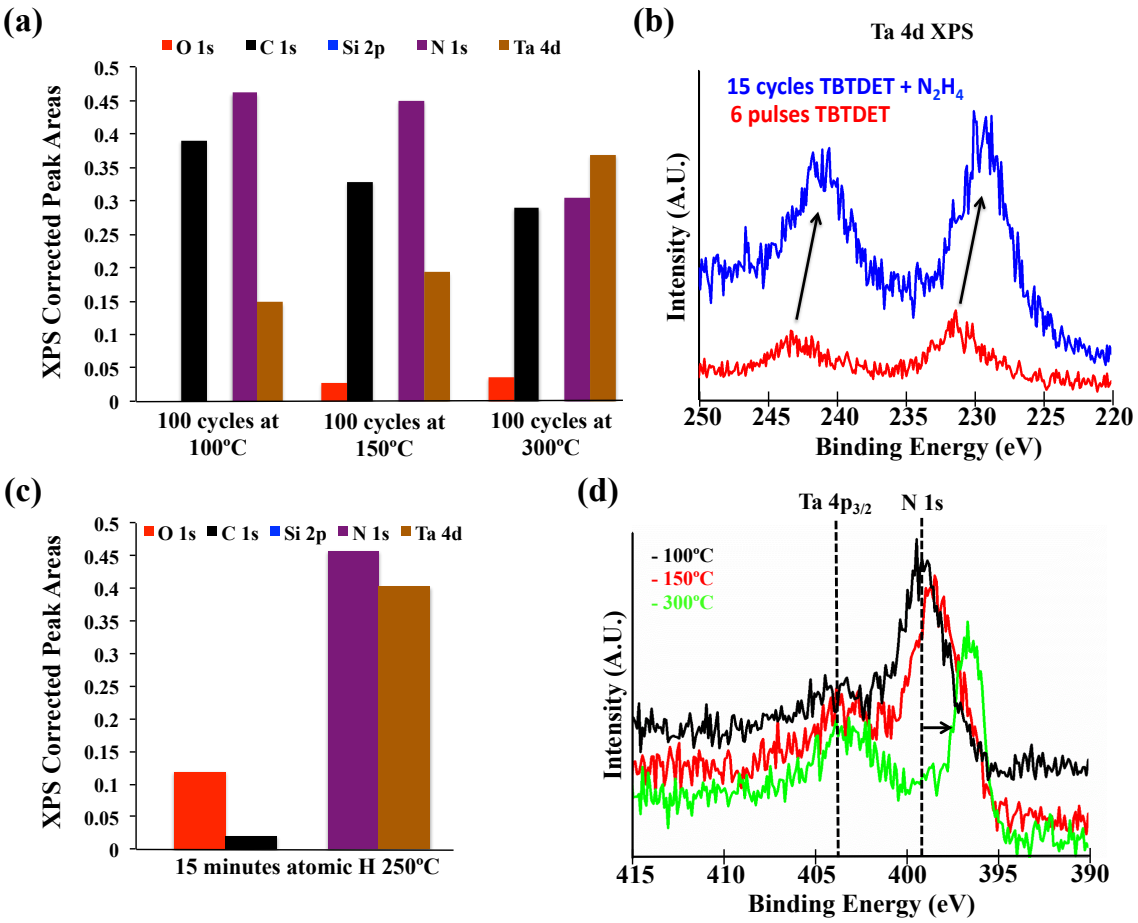

Figure 3.3: TaN_x deposition from TBTDET + N_2H_4. a) XPS of 100 cycles of TBTDET and N_2H_4 at 100ºC, 150ºC, and 300ºC. b) The Ta 4d XPS peaks after 6 pulses of TBTDET and after 15 TaN_x cycles. The initial 6 pulses confirmed interfacial Si-O-Ta bond formation, while after 15 cycles an ~2eV shift is seen consistent with formation of Ta-N bonds. (c) 15 minutes of atomic H were enough to remove the carbon that was accumulating on the surface during deposition. (d) Ta $4p_{3/2}$ / N 1s region showing the N 1s component shifting and narrowing as a function of ALD temperature.

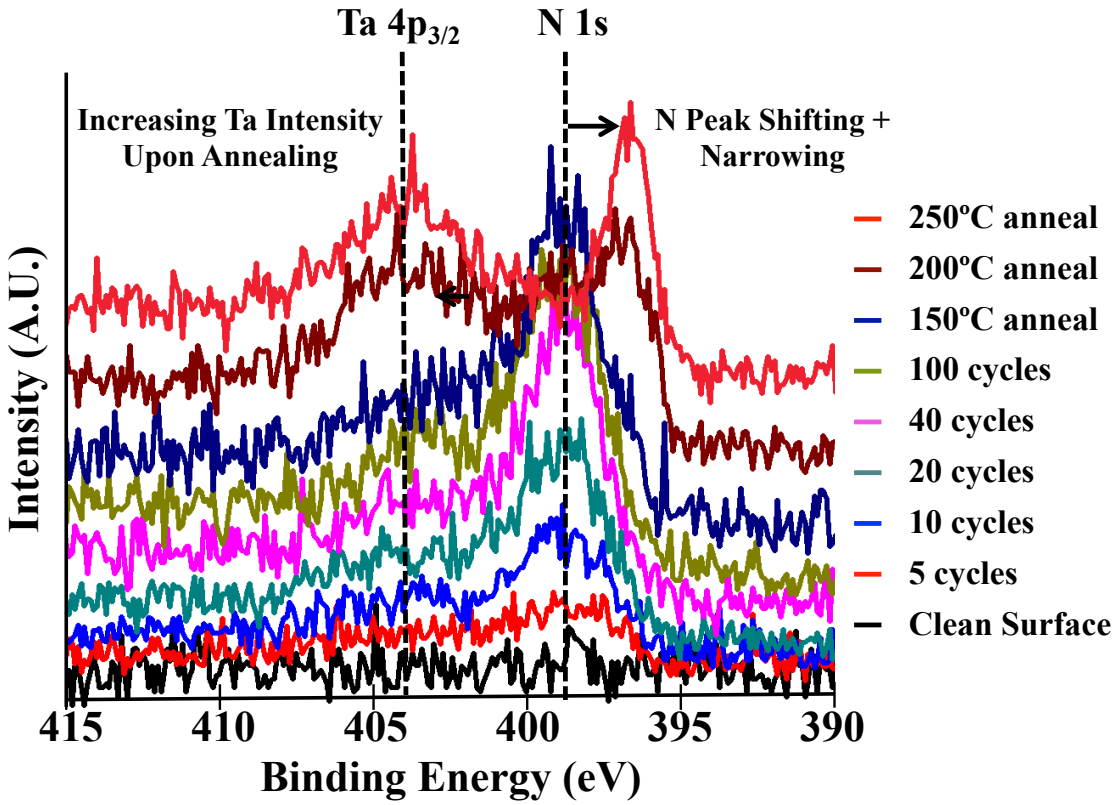

Figure 3.4: XPS of TaN_x Cycles at 100ºC and Post Deposition Anneal (PDA). XPS was performed after subsequent cycles of TaN_x ALD at 100ºC. After 100 total cycles, a 150ºC, 200ºC, and 250ºC anneal were performed each for 30 minutes. Note the shift in the N 1s peak, as well as additional intensity in the Ta $4p_{3/2}$ component upon annealing.

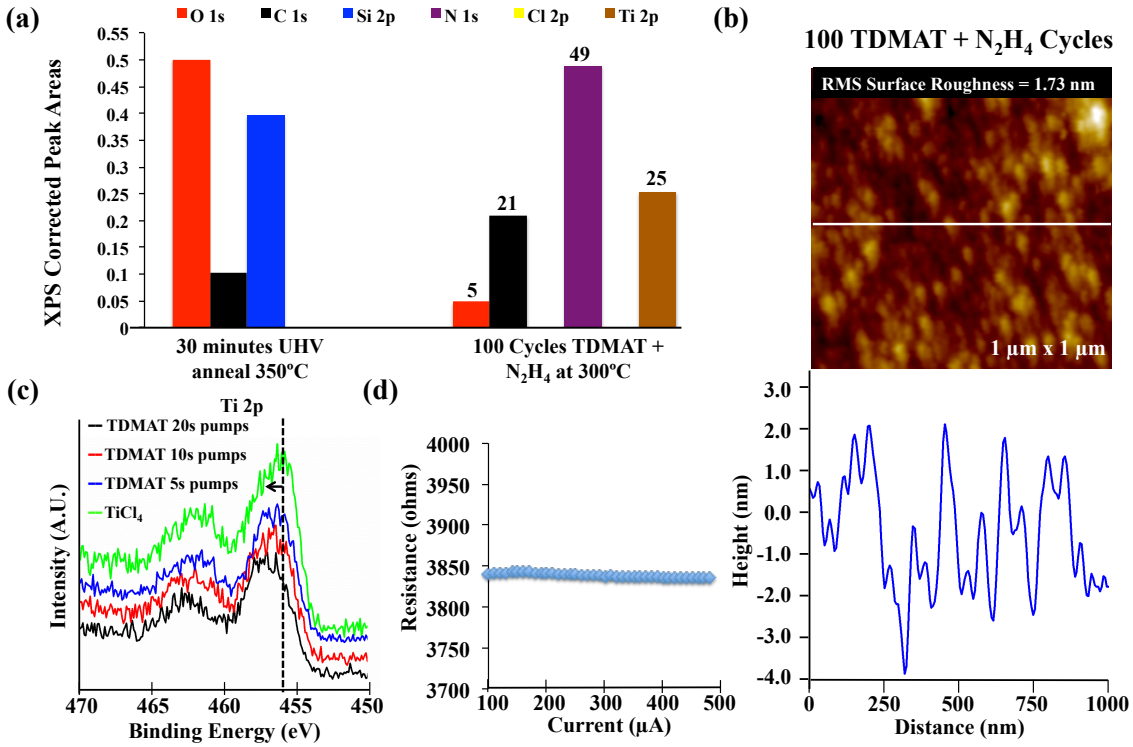

Figure 3.5: TDMAT Grown TiN_x Films. (a) XPS and (b) AFM of 100 cycles TiN_x at 300ºC grown with N_2H_4. c) The Ti 2p peak positions as a function of TDMAT pump time before N_2H_4 exposure. The position is compared to $TiCl_4$ processing. d) Resistance measurement of TDMAT grown films with a 5 second pump.

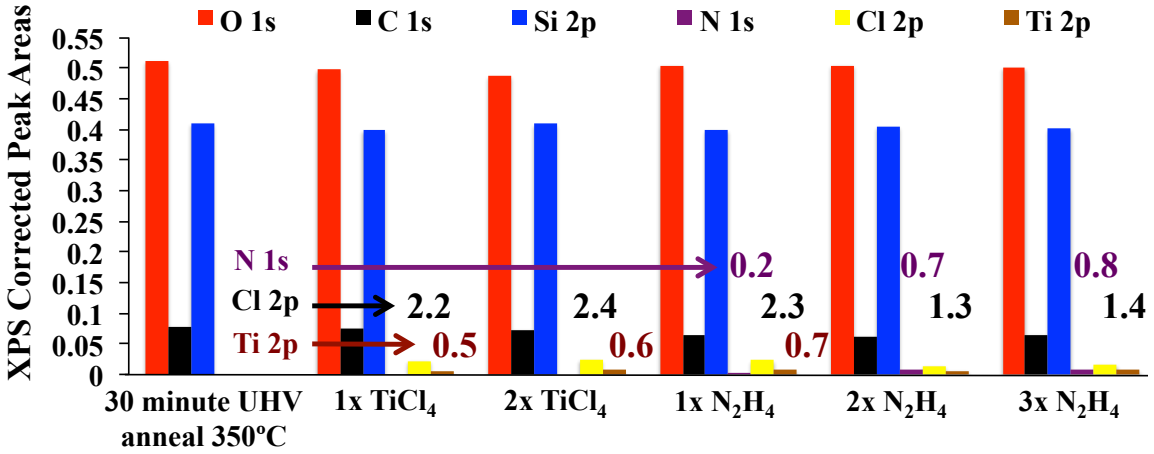

Figure 3.6: XPS Saturation Study of $TiCl_4$ and N_2H_4 on Clean SiO_2 at 300ºC. Initial 1x $TiCl_4$ dose deposited 2.2% Cl and 0.5% Ti on UHV annealed SiO_2/Si. Additional 2x $TiCl_4$ saturated Cl at 2.4% and Ti at 0.6%. Similarly, a 1x, 2x, and 3x dose of N_2H_4 were performed, which saturated the Cl at 1.4% and N at 0.8%. Self-limiting exposures were consistent with ALD.

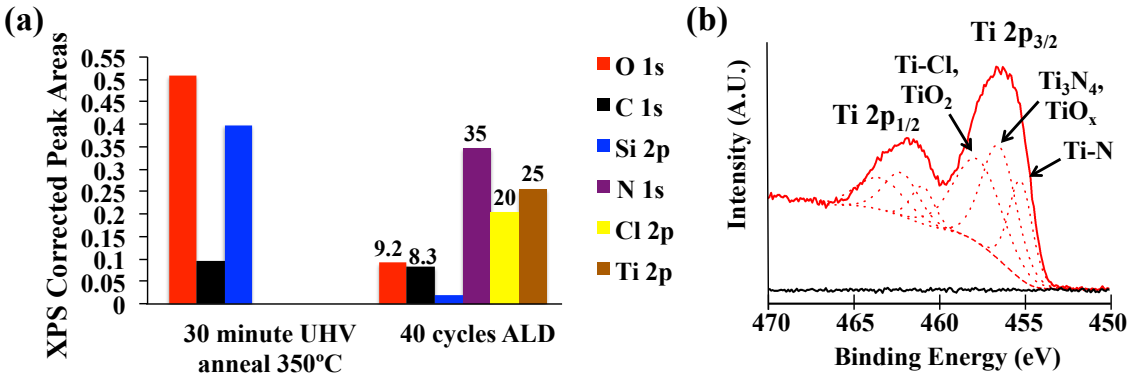

Figure 3.7: Growth of TiN_x Film at 300ºC. a) Normalized and corrected XPS of 40 cycles TiN_x at 300ºC on a UHV annealed surface. The 300ºC film contains significant Cl residue. b) Raw XPS outlining the various components that are present in the Ti 2p spectra.

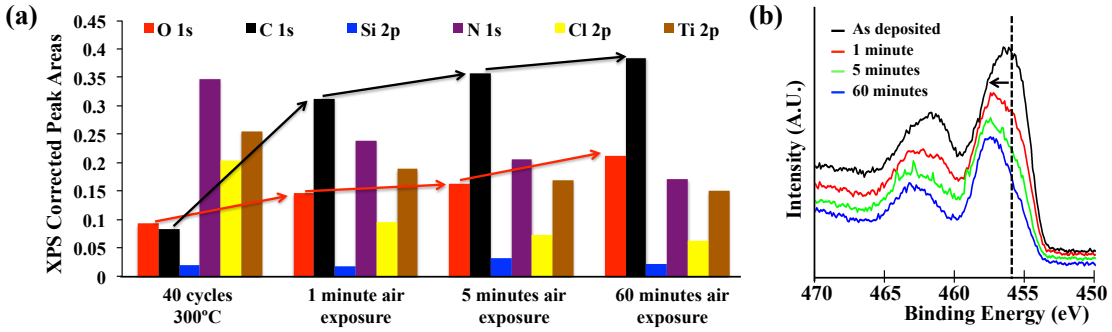

Figure 3.8: Effect of Air Exposure. a) 40 cycles TiN_x at 300ºC followed by 1 minute, 5 minutes, and 60 minutes of air exposure. b) Ti 2p raw XPS peaks showed an ~1.5 eV BE shift after just 1 minute of air exposure. After 1 hour, the TiN component located at 455eV was significantly reduced.

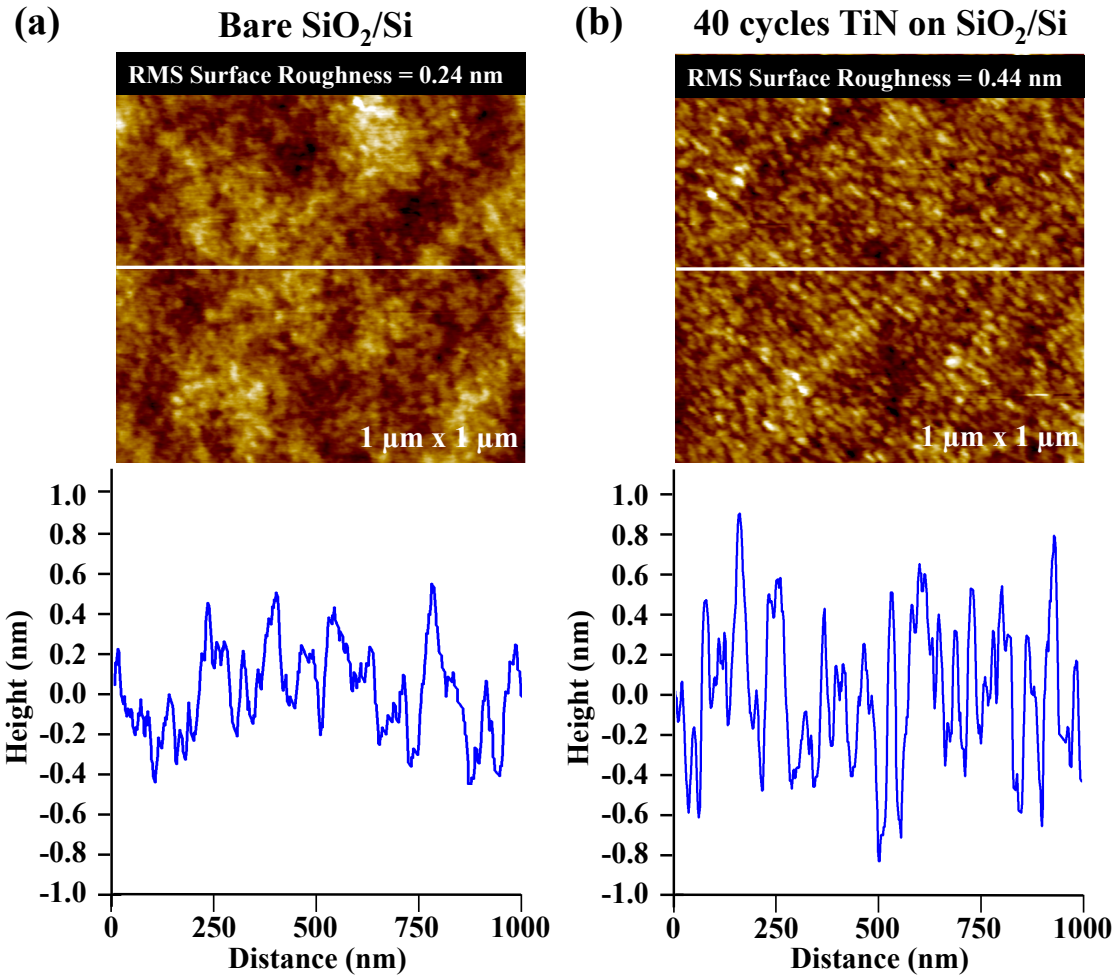

Figure 3.9: *Ex Situ* AFM Imaging. a) Bare SiO_2 and b) 40 cycles $TiCl_4$ + N_2H_4 at 300ºC. The low RMS surface roughness was indicative of conformal TiN_x growth.

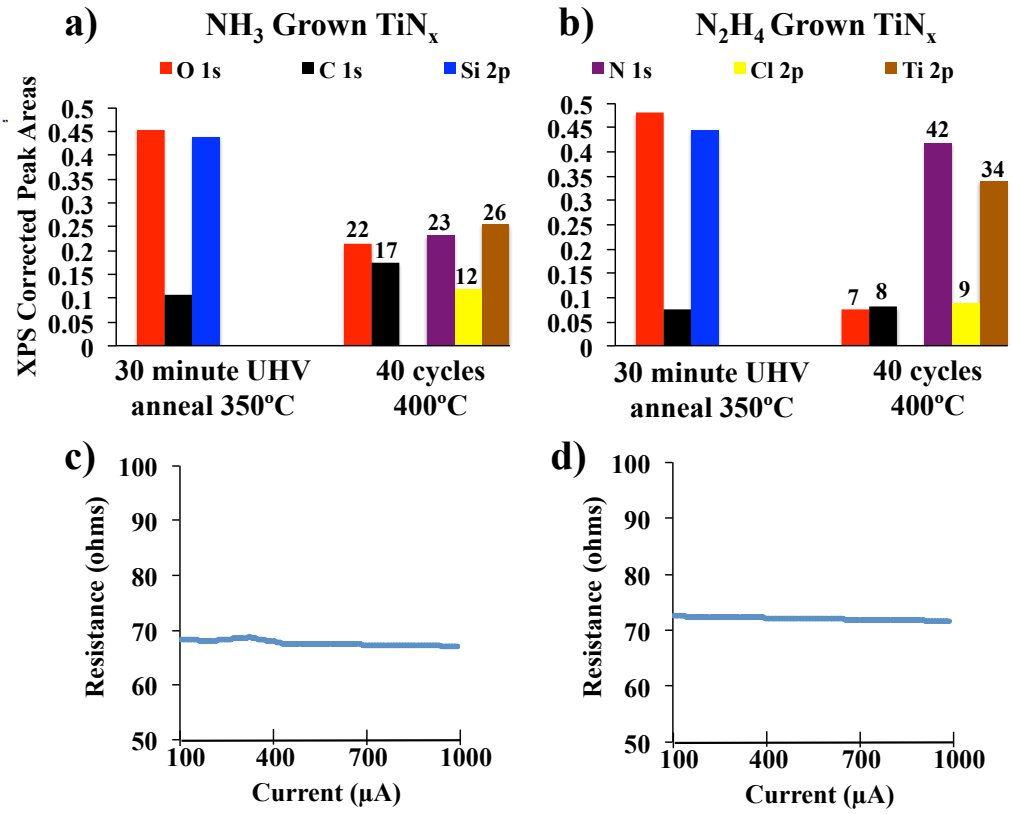

Figure 3.10: NH_3 vs. N_2H_4 Grown TiN_x Films. 40 cycles TiN_x at 400ºC grown with a) NH_3 and b) N_2H_4. The amount of O and C was ~2x larger with the Cl being 50% higher in NH_3 grown films. Resistance measurements for c) NH_3 and d) N_2H_4 grown TiN_x films.

Table 3.1: Summary of TiN_x Films Grown with NH_3 and N_2H_4.

Nitrogen Precursor	Temperature (°C)	Residual Chlorine (%)	Number of Cycles	SEM Thickness	Growth Rate (nm/cycle)	Resistivity (μohm-cm)
NH_3	300	16.0	80	13	0.16	2,885
NH_3	400	12.1	40	18	0.45	554
N_2H_4	300	18.1	80	17	0.21	593
N_2H_4	400	8.7	40	11	0.28	359

3.8 References

1. K. E. Elers, V. Saanila, P. J. Soininen, W. M. Li, J. T. Kostamo, S. Haukka, J. Juhanoja, W. F. Besling, Diffusion barrier deposition on a copper surface by atomic layer deposition. *Chemical Vapor Deposition* **8**, 149-153 (2002).

2. H. O. Pierson, *Handbook of Refractory Carbides & Nitrides: Properties, Characteristics, Processing and Apps*. (William Andrew, 1996).

3. A. Sidhwa, C. Spinner, T. Gandy, W. Brown, S. Ang, H. Naseem, R. Ulrich, Evaluation of Contact and Via Step Coverage Using a Novel Two-Step Titanium Nitride Barrier Deposition Process. *MRS Proceedings* **716**, B12.10 (2011).

4. J. Xiang, T. Li, X. Wang, K. Han, J. Li, C. Zhao, Understanding the role of TiN barrier layer on electrical performance of MOS device with ALD-TiN/ALD-TiAlC metal gate stacks. *ECS Journal of Solid State Science and Technology* **5**, P327-P329 (2016).

5. F. Chen, O. Bravo, K. Chanda, P. McLaughlin, T. Sullivan, J. Gill, J. Lloyd, R. Kontra, J. Aitken, in *Reliability Physics Symposium Proceedings, 2006. 44th Annual., IEEE International*. (IEEE, 2006), pp. 46-53.

6. H.-J. Lee, J.-S. Park, S.-H. Kwon, Plasma-enhanced atomic layer deposition of tantalum nitride thin films using tertiary-amylimido-tris(dimethylamido)tantalum and hydrogen plasma. *Journal of Electroceramics* **36**, 165-169 (2016).

7. M. Ritala, P. Kalsi, D. Riihelä, K. Kukli, M. Leskelä, J. Jokinen, Controlled Growth of TaN, Ta3N5, and TaO x N y Thin Films by Atomic Layer Deposition. *Chemistry of materials* **11**, 1712-1718 (1999).

8. H.-S. Chung, J.-D. Kwon, S.-W. Kang, Plasma-Enhanced Atomic Layer Deposition of TaN Thin Films Using Tantalum-Pentafluoride and N2⁄ H2⁄ Ar Plasma. *Journal of The Electrochemical Society* **153**, C751-C754 (2006).

9. M. Ritala, M. Leskelä, E. Rauhala, J. Jokinen, Atomic Layer Epitaxy Growth of TiN Thin Films from Til4 and NH3. *Journal of the Electrochemical Society* **145**, 2914-2920 (1998).

10. B. Burton, A. Lavoie, S. George, Tantalum nitride atomic layer deposition using (tert-Butylimido) tris (diethylamido) tantalum and hydrazine. *Journal of the Electrochemical Society* **155**, D508-D516 (2008).

11. J. Elam, M. Schuisky, J. D. Ferguson, S. George, Surface chemistry and film growth during TiN atomic layer deposition using TDMAT and NH3. *Thin Solid Films* **436**, 145-156 (2003).

12. J.-S. Min, Y.-W. Son, W.-G. Kang, S.-S. Chun, S.-W. Kang, Atomic layer deposition of TiN films by alternate supply of tetrakis (ethylmethylamino)-titanium and ammonia. *Japanese journal of applied physics* **37**, 4999 (1998).

13. J. Musschoot, Q. Xie, D. Deduytsche, S. Van den Berghe, R. Van Meirhaeghe, C. Detavernier, Atomic layer deposition of titanium nitride from TDMAT precursor. *Microelectronic Engineering* **86**, 72-77 (2009).

14. M. Burke, A. Blake, I. M. Povey, M. Schmidt, N. Petkov, P. Carolan, A. J. Quinn, Low sheet resistance titanium nitride films by low-temperature plasma-enhanced atomic layer deposition using design of experiments methodology. *Journal of Vacuum Science & Technology A: Vacuum, Surfaces, and Films* **32**, 031506 (2014).

15. F. Andrieu, O. Faynot, X. Garros, D. Lafond, C. Buj-Dufournet, L. Tosti, S. Minoret, V. Vidal, J. Barbe, F. Allain, in *Electron Devices Meeting, 2006. IEDM'06. International*. (IEEE, 2006), pp. 1-4.

16. K. Choi, H.-C. Wen, H. Alshareef, R. Harris, P. Lysaght, H. Luan, P. Majhi, B. Lee, in *Solid-State Device Research Conference, 2005. ESSDERC 2005. Proceedings of 35th European*. (IEEE, 2005), pp. 101-104.

17. K.-E. Elers, J. Winkler, K. Weeks, S. Marcus, TiCl4 as a precursor in the TiN deposition by ALD and PEALD. *Journal of the Electrochemical society* **152**, G589-G593 (2005).

18. J. Suehle, E. Vogel, M. Edelstein, C. Richter, N. Nguyen, I. Levin, D. Kaiser, H. Wu, J. Bernstein, in *Plasma-and Process-Induced Damage, 2001 6th International Symposium on*. (IEEE, 2001), pp. 90-93.

19. D. Alvarez, J. Spiegelman, R. Holmes, K. Andachi, M. Raynor, H. Shimizu, Ultra-High Purity Hydrazine Delivery for Low Temperature Metal Nitride ALD. *ECS Transactions* **77**, 219-225 (2017).

20. J. G. Speight, *Lange's handbook of chemistry*. (McGraw-Hill New York, 2005), vol. 1.

21. M. Edmonds, K. Sardashti, S. Wolf, E. Chagarov, M. Clemons, T. Kent, J. H. Park, K. Tang, P. C. McIntyre, N. Yoshida, Low temperature thermal ALD of a SiNx interfacial diffusion barrier and interface passivation layer on SixGe1− x (001) and SixGe1− x (110). *The Journal of Chemical Physics* **146**, 052820 (2017).

22. S. Wolf, M. Edmonds, K. Sardashti, M. Clemons, J. H. Park, N. Yoshida, L. Dong, S. Nemani, E. Yieh, R. Holmes, Low-Temperature Amorphous Boron

Nitride on Si 0.7 Ge 0.3 (001), Cu, and HOPG from Sequential Exposures of N2 H4 and BCl 3. *Applied Surface Science*, (2018).

23. N. C. Saha, H. G. Tompkins, Titanium nitride oxidation chemistry: An x‐ray photoelectron spectroscopy study. *Journal of Applied Physics* **72**, 3072-3079 (1992).

24. D. Sarma, C. Rao, XPES studies of oxides of second-and third-row transition metals including rare earths. *Journal of Electron Spectroscopy and Related Phenomena* **20**, 25-45 (1980).

25. H. Demiryont, J. R. Sites, K. Geib, Effects of oxygen content on the optical properties of tantalum oxide films deposited by ion-beam sputtering. *Applied Optics* **24**, 490-495 (1985).

26. J.-S. M. Lehn, P. van der Heide, Y. Wang, S. Suh, D. M. Hoffman, A new precursor for the chemical vapor deposition of tantalum nitride films. *Journal of Materials Chemistry* **14**, 3239-3245 (2004).

27. J.-S. Park, M.-J. Lee, C.-S. Lee, S.-W. Kang, Plasma-enhanced atomic layer deposition of tantalum nitrides using hydrogen radicals as a reducing agent. *Electrochemical and Solid-State Letters* **4**, C17-C19 (2001).

28. S. Hofmann, The contribution of characteristic energy losses in the core-level X-ray photoelectron spectroscopy peaks of TiN and (Ti, Al) N studied by electron energy loss spectroscopy and X-ray photoelectron spectroscopy. *Journal of Electron Spectroscopy and Related Phenomena* **56**, 85-103 (1991).

29. B. J. Burrow, A. E. Morgan, R. C. Ellwanger, A correlation of Auger electron spectroscopy, x‐ray photoelectron spectroscopy, and Rutherford backscattering spectrometry measurements on sputter‐deposited titanium nitride thin films. *Journal of Vacuum Science & Technology A: Vacuum, Surfaces, and Films* **4**, 2463-2469 (1986).

30. J. Sullivan, S. Saied, I. Bertoti, Effect of ion and neutral sputtering on single crystal TiO2. *Vacuum* **42**, 1203-1208 (1991).

31. I. Bertoti, M. Mohai, J. Sullivan, S. Saied, Surface characterisation of plasma-nitrided titanium: an XPS study. *Applied surface science* **84**, 357-371 (1995).

32. C. Mousty‐Desbuquoit, J. Riga, J. J. Verbist, Solid state effects in the electronic structure of TiCl4 studied by XPS. *The Journal of Chemical Physics* **79**, 26-32 (1983).

33. D. Fregonese, A. Glisenti, S. Mortara, G. A. Rizzi, E. Tondello, S. Bresadola, MgCl2/TiCl4/AlEt3 catalytic system for olefin polymerisation: a XPS study. *Journal of Molecular Catalysis A: Chemical* **178**, 115-123 (2002).

34. H. Kondo, K. Furumai, M. Sakashita, A. Sakai, S. Zaima, Thermal Stability and Scalability of Mictamict Ti–Si–N Metal–Oxide–Semiconductor Gate Electrodes. *Japanese Journal of Applied Physics* **48**, 04C012 (2009).

35. E. Langereis, H. Knoops, A. Mackus, F. Roozeboom, M. Van de Sanden, W. Kessels, Synthesis and in situ characterization of low-resistivity Ta N x films by remote plasma atomic layer deposition. *Journal of Applied Physics* **102**, 083517 (2007).

36. P. Caubet, T. Blomberg, R. Benaboud, C. Wyon, E. Blanquet, J.-P. Gonchond, M. Juhel, P. Bouvet, M. Gros-Jean, J. Michailos, Low-temperature low-resistivity PEALD TiN using TDMAT under hydrogen reducing ambient. *Journal of The Electrochemical Society* **155**, H625-H632 (2008).

37. B.-Y. Kim, S.-H. Lee, S.-G. Park, K.-Y. Oh, J. Song, D.-H. Kim, Comparison study for TiN films deposited from different method: chemical vapor deposition and atomic layer deposition. *MRS Online Proceedings Library Archive* **672**, (2001).

Chapter 4

The Role of Oxide Formation on Selective Co and Ru Metal ALD

4.1 Abstract

Advanced interconnect materials replacing Cu include Co and Ru, particularly at early metallization steps in small vias where Cu resistivity increases due to grain boundary scattering. In this study, hyper-selective Co ALD was performed from Bis(1,4-di-tert-butyl-1,3-diazadienyl) cobalt [$Co(dad)_2$] and two co-reactants (formic acid [HCOOH] and tert-butylamine [TBA]). Utilizing HCOOH, *in situ* XPS showed no deposition on SiO_2 and thick films on Pt consistent with infinite selectivity; however, Cu etching was observed. By switching to TBA, no etching and similar metallic Co films were achieved with only 4% CoO_x on SiO_2 independent of the number of ALD cycles. Co scavenged weakly bound oxygen from under-coordinated sites on SiO_2 leading to an unreactive oxidic particulate. These co-reactants were also employed with a Ru precursor: η^4-2,3-dimethylbutadiene ruthenium tricarbonyl [$RuDMBD(CO)_3$]. Selective deposition on metals vs. SiO_2 with sub-1 nm roughness in AFM was achieved; however, the formation of sub-stoichiometric RuO_x on SiO_2 was unable to inhibit further deposition consistent with the $RuDMBD(CO)_3$ precursor being low valent and Ru being less prone to oxidation than Co. The results revealed that metal ALD can be self-limiting on oxides if the metal is able to fully oxidize; this is an especially robust type of passivant-free selectivity.

4.2 Introduction

As the scaling of transistors continues so does the need for depositing conductive interconnect metal in shrinking vias. It is desired to have selective metal deposition for bottom-up fill for both middle-of-line (MOL or MEOL) and back end-of-line (BEOL) processing. This would induce the formation and growth of larger grains, which are expected to decrease via and interconnect resistance by reducing grain boundaries and decreasing surface roughness (see Fig. 4.1). This scattering has been well documented and simulated for current Cu interconnects (*1-3*). In addition, bottom-up atomic layer deposition (ALD) growth is the preferred deposition method since it should prevent keyhole and seam formation in tight geometries and high aspect ratio features. The key advanced metals for bottom-up growth include cobalt (*4*) and ruthenium (*5*). Cobalt is particularly important since it used as both a capping layer on Cu to protect it from oxidation (*6*), and in sub-10 nm vias, where Co is considered to be a better conductor than Cu due to Co having a smaller electron mean free path and problems with Cu electroplating in sub-10 nm vias (*7, 8*).

Conductive Co has previously been reported by the Winter group and was grown via ALD using Bis(1,4-di-tert-butyl-1,3-diazadienyl) cobalt [$Co(dad)_2$] and formic acid (HCOOH) and tert-butylamine (TBA) at temperatures near 180ºC with high selectivity but were not studied with *in situ* XPS (*9, 10*). Additionally, the mechanism of selectivity was presumed to be precursor decomposition by catalysis on metallic surfaces. Other recent work involving $Co(dad)_2$ was performed by Kim *et al* who used ozone as a co-reactant, but was only able to achieve cobalt oxide films at 120ºC (*11*). Ozone as a co-reactant is corrosive to Cu interconnects (*12, 13*); therefore, exploring and discovering

co-reactants that are not caustic to Cu are crucial. This study seeks to understand the mechanism for Co and Ru metal selectivity using *in situ* XPS, and ultimately determine the role of oxide formation on insulators that results in infinite selectivity.

Extension of the co-reactants TBA and HCOOH were applied to ALD with a Ru precursor, η^4-2,3- dimethylbutadiene ruthenium tricarbonyl [RuDMBD$(CO)_3$]. Previous reports show that this precursor can react with O_2 and plasma O_2 at elevated temperatures (>220ºC) to form ruthenium metal or ruthenium oxide depending on the temperature and amount of oxygen dosed per cycle (*14*). Additionally, resistivities of these films were reported as low as 13.7 μohm-cm after a post-deposition anneal (*15*). More recent work has also seen ALD using RuDMBD$(CO)_3$ with H_2O at lower temperatures (*16*), but no reference to selective deposition has been reported. Khan *et al* have used dicarbonyl-bis(5-methyl-2,4-hexanediketonato)Ru and O_2 at 283ºC to selectively deposit Ru; however, the use of an inhibitor was necessary to achieve about 10 nm of selectivity (*17*). In the present study, the authors are reporting a novel selective Ru ALD that has been achieved on metals vs. insulating substrates as function of controlling the temperature and by using HCOOH or TBA as a co-reactant.

4.3 Experimental

ALD cobalt metal was explored using a metal-organic cobalt precursor, [Co$(dad)_2$], and either a co-reactant of HCOOH or TBA at 180ºC on Cu, Pt, and SiO_2 substrates. Similarly Ru, films were deposited at temperatures between 100ºC and 325ºC with HCOOH and TBA to determine the selectivity window. The deposited Co films were studied using *in situ* x-ray photoelectron spectroscopy (XPS) and atomic force

microscopy (AFM). Cross-sectional scanning electron microscopy (SEM) was used to check the film thicknesses to estimate a growth per cycle.

Cu and Pt samples used in this study were grown by DC magnetron sputtering on SiO_2 substrates consisting of 300 nm of thermal SiO_2 on Si(001) (University Wafer). Samples underwent an *ex situ* degrease involving rinses in acetone, methanol, and water before being rapidly loaded into the vacuum chamber (<5 min). Once loaded into the load lock chamber, the samples were transferred into the UHV chamber and typically heated to 350°C for 30 minutes to produce clean starting substrates. Precursor exposures were performed in a deposition chamber, as shown in Fig 4.2. The deposition chamber and dosing lines were pumped with a turbomolecular pump producing a base pressure of ~$5x10^{-7}$ Torr. The chamber was heated ~125°C, and dosing lines were kept ~10-20ºC warmer than precursor containers to ensure precursors would not condense in the lines. The $Co(dad)_2$ precursor was heated to 150ºC and was used with ultrahigh purity N_2 that was passed through a purifier to act as a push gas for the delivery of the $Co(dad)_2$ to the samples. $RuDMBD(CO)_3$ was supplied by EMD and gently heated to 30ºC. TBA and HCOOH (Sigma Aldrich) were used as received and dosed at room temperature. No purge gas was employed to reduce any surface contamination/oxygen incorporation into the films. Before moving samples into the deposition chamber, they were preheated in the UHV chamber via a pyrolytic boron nitride heater. For the ALD, samples were heated via an enclosed cartridge heater to eliminate hot wire reactions and minimize CVD, which would lead to improved selectivity. After deposition, samples were transferred back to the UHV chamber where *in situ* x-ray photoelectron spectroscopy (XPS) was performed without breaking vacuum. A monochromatic XPS system (Al kα hν = 1486.7

eV) was employed to collect surface-sensitive spectra at an angle of 30° with respect to the surface parallel. An electron pass energy of 50 eV and a line width of 0.1 eV were used for collection, and CASA XPS v.2.3 utilizing Shirley background subtractions was used for analysis. Relative sensitivity factors (Schofield) were used to correct raw peak areas before normalization and final quantification. In addition to XPS, surface topography was characterized with AFM and samples thick enough were analyzed with cross-sectional SEM.

4.4 Hyper-Selective Co ALD

4.4.1 Deposition with HCOOH

Nearly infinite selective deposition of Co on a conductor and not an SiO_2 was observed for 180ºC ALD with $Co(dad)_2$ and HCOOH. Fig. 4.3 plots the normalized XPS data after 100 ALD cycles followed by an additional 100 cycles on UHV annealed Pt vs SiO_2. Pt was employed since it is not etched by HCOOH. On Pt, a thick (>10 nm) Co^{+0} film was deposited while virtually no deposition occurred on SiO_2. The raw binding energy peaks of the Co spectra on Pt and SiO_2 are plotted in Figs. 4.3C and 4.3D, respectively. The metallic Co $2p_{3/2}$ signal on Pt had a binding energy of ~778eV consistent with previous reports for metallic Co (*18, 19*), while there was no detectable Co 2p signal on SiO_2 after deposition.

AFM images showed no change on SiO_2 before and after Co ALD cycles consistent with no nuclei formation, while the Co on Pt surface roughness remains below 1.8 nm (Fig. 4.4). The brighter white-colored dots observed on SiO_2 before and after deposition did not significantly change and can be attributed to hydrocarbon

contamination from ambient exposure; these features were ~ 2-3 nm tall before and after deposition. On Pt, the imaging indicated a low density of pits consistent with depositing Co on a significant carbon component as seen in XPS; plasma pre-clean should eliminate these features by reducing the carbon on the starting surface allowing for better nucleation and growth.

To verify self-limiting precursor exposures consistent with ALD, a saturation study was performed and monitored with XPS; Fig. 4.5A highlights the effect of individual additional half cycle amounts that resulted in self-limiting $Co(dad)_2$ and HCOOH exposures confirming ALD behavior. Essentially, 1 pulse (1 second exposure) of each precursor was followed by 2 additional pulses of the same precursor (2 seconds) to confirm self-limiting behavior in XPS peak areas. Additionally, this study revealed a novel mechanism about the reaction. Previously it was thought that the HCOOH dissociatively chemisorbed to produce atomic H which removed the ligands from $Co(dad)_2$. Instead, XPS indicated that HCOOH did not remove the ligands but instead induced a ligand-exchange process. Fig. 4.5B shows the Co 2p peak that indicated the HCOOH induced a higher binding energy component consistent with a formate on the surface that was subsequently removed upon exposure to $Co(dad)_2$.

4.4.2 Selective Co from TBA

Deposition with HCOOH was attempted on Cu substrates (Fig. 4.6A); however, the Cu substrate signal never decreased to zero, consistent with etching by HCOOH. Therefore, an alkyl amine co-reactant (TBA) was also studied (Fig. 4.6B). For $Co(dad)_2$ + TBA ALD at 180ºC, reduced Co metal films were deposited on Cu and Pt substrates with

hyper-selectivity against SiO_2. Films as thick as 30 nm were grown on the conductors while completely attenuating the substrate Cu 2p peaks consistent with zero etching of Cu. On SiO_2, only 4% CoO_x was deposited after an initial 50 ALD cycles. After an additional 250 ALD cycles, there was still only 4% CoO_x indicative of saturation and hyper-selectivity due to a self-limiting growth on the oxide (Fig. 4.7B). The Co $2p_{3/2}$ signal on SiO_2 was highly shifted in comparison to the signal on Cu (Fig. 4.7C and 4.7D). This shifted signal on SiO_2 had a peak position at ~782eV, corresponding to a very oxygen rich, and likely stoichiometric Co_2O_3 or Co_3O_4 (*20, 21*). A similar saturation study for Co grown with TBA was performed.

AFM imaging and corresponding line trace data from 300 cycles of ALD with TBA confirmed smooth films with low surface roughness on Pt and Cu. After deposition on SiO_2, small (<5 nm tall and ~5-10 nm wide) CoO_x particles were present on SiO_2 (Fig. 4.8), which corresponds to the CoO_x observed in the Co 2p XPS spectra.

To check for the bottom-up fill nature of Co using the TBA process, 3000 cycles of ALD was performed on a patterned sample from Applied Materials consisting of SiCOH/SiN sidewalls with Cu at the bottom of vias (Fig. 4.9). The patterned sample underwent a 300ºC atomic H clean to ensure maximum cleanliness without damaging the low-k material. The amount of Cu on the patterned sample was <1% (Fig. 4.9A) even by performing XPS analysis at 90º; however, the oxidation state was consistent with metallic Cu (shifted due to the effect of surface charging) after the H clean (Fig. 4.9B). The 3000 cycles of ALD was infinitely selective to the insulating SiCOH and SiN. Moreover, the cobalt began growing up from the metallic Cu. Approximately 12 nm of Co was grown bottom-up; however, the expected thickness was on the order of 100 nm. It was

hypothesized that the porous SiCOH can poison the growth by allowing oxygen/water to diffuse out and oxidize the cobalt. Once oxidation occurs, further deposition was inhibited; therefore, metallic Co must be restored prior to additional deposition with this process. It should be noted that the atomic hydrogen clean was proven not to damage the SiCOH so it can be employed for the *in situ* clean.

4.5 Ru ALD

Ru metal ALD was performed with $RuDMBD(CO)_3$ and either HCOOH or TBA. It was observed that at a sample temperature of 325ºC, unselective growth of Ru was achieved on all surfaces. Likewise, when the sample temperature was set to 100ºC and the Ru ALD performed, there was no deposition. However, ALD at 215ºC resulted in selectivity of about 1.8 nm on Cu to 0.2 nm on SiO_2 when using TBA as a co-reactant. Further dropping the temperature to 200ºC resulted in slightly better selectivity, but decreased the growth rate by nearly a factor of four (Fig. 4.10). Similar selectivity was observed for HCOOH; however, similar to the Co ALD with HCOOH, AFM imaging after $RuDMBD(CO)_3$ and HCOOH showed rough films on Cu with an RMS surface roughness of nearly 10 nm consistent with etching. By using the more-gentle TBA, the deposited films in AFM were very flat with a surface roughness of less than 1 nm consistent with the absence of etching (Fig. 4.11).

To understand the nature of the selectivity, the raw elemental Ru 3d peaks are plotted in Fig. 4.12. Fig. 4.12A shows the Ru 3d peak for deposition on SiO_2, while Fig. 4.12B shows the deposition on the conductors. It was observed that the Ru $3d_{5/2}$ peak had a position of ~280.3 eV for Ru grown on the oxide, whereas the peak position for growth

on Pt and Cu was ~279.8 eV. These binding energies differ by only 0.5 eV; in the literature metallic Ru has been reported at values most commonly ranging from 279.9 eV to about 280.1 eV(*22-24*). As for ruthenium oxides, values as high as ~283 eV have been reported for ruthenium in +3 and +4 oxidation states (*24, 25*). Observing a peak position nearly 2.5 eV lower than reported values is consistent with a sub-stoichiometric RuO_x (*25*). It should also be noted that there is a small C 1s overlap with the Ru $3d_{3/2}$ component.

4.6 Discussion and Conclusion

The mechanism of selectivity between the Co and Ru processes has been studied with XPS. For Co ALD, XPS saturation studies with HCOOH and TBA indicate a ligand exchange mechanism. As shown in Fig 4.5. dosing HCOOH clearly increased the C, O, and shifted higher BE components of C and Co on the surface. Ending with a $Co(dad)_2$ pulse removes the higher BE formate on the surface inducing the formation of a volatile reaction byproduct. This was consistent with $Co(dad)_2$ promoting the dissociation of the formate ligand from the surface and ultimately driving the formation of a volatile specie(s) that are pumped away. In a similar manner, when TBA was used as a co-reactant, the C and N increase after TBA dosing, and were reduced after $Co(dad)_2$ dosing. This reaction was again consistent with a ligand exchange reaction occurring on the surface (Fig. 4.13).

As for the Ru ALD process, a slightly different mechanism is thought to occur due to inherent differences with the precursor being low valent and processing dissimilar ligands. When the $RuDMBD(CO)_3$ is introduced to the surface, the CO termination

remains intact, but the weakly bound butadiene is able to dissociate and pump away. When the TBA is then introduced to the surface, the amine can react with the carbonyls inducing the formation of a volatile reaction byproduct that leaves the surface terminated with metallic Ru (Fig. 4.14).

The Co process is inherently more selective than the Ru process because of the formation of a very oxygen-rich CoO_x. The peak position between metallic Co grown on Pt/Cu and the oxidized Co grown on SiO_2 was nearly 4eV with TBA. With HCOOH grown Co ALD, no CoO_x nuclei are hypothesized to have formed on SiO_2 due to likely etching by the HCOOH. In comparison, the Ru grown on Pt/Cu vs. SiO_2 was only 0.5 eV. This small difference means the sub-oxide of Ru is likely still conductive and able to continue the ALD reaction. Two factors are hypothesized to result in the lack of more oxygen-rich RuO_x formation: (a) The Ru precursor is low valent and (b) RuO_4 and even RuO_2 have heats of formation of -239 kJ/mol (*26*) and -315 kJ/mol (*27*), respectively, per Ru atom. Co_3O_4 has a heat of formation of -910 kJ/mol (*28*) that corresponds to -455 kJ/mol per Co atom. Therefore Co has a much stronger tendency to react with more weakly bound, under-coordinated oxygen on SiO_2. In order to achieve better selectivity, formation of a more oxygen-rich RuO_x is necessary consistent with the higher selectivity observed when using a Ru precursor, which has a Ru:O ratio of 4 such as dicarbonyl-bis(5-methyl-2,4-hexanediketonato)Ru (*17*). Similarly, RuO_4, as fairly recently used by Minjauw *et al* (*29*), may display improved selectivity.

The novel Ru ALD selectivity was limited due to the formation of a sub-stoichiometric RuO_x that was not as inhibitive to further deposition. To further improve the selectivity on Cu, use of oxygen-rich Ru precursor is needed since an oxidizing co-

reactant must be avoided for interconnects. Hyper-selective Co metal deposition was produced from $Co(dad)_2$ and both co-reactants (HCOOH and TBA). Utilizing HCOOH, no deposition was seen on SiO_2 consistent with infinite deposition, however HCOOH was observed to etch Cu. By switching to TBA, no Cu etching was observed, a crucial restraint to be compatible with existing MEOL and BEOL processing, and similar metallic Co films were deposited with only 4% CoO_x on SiO_2 independent of the number of Co ALD cycles. The self-limiting deposition on SiO_2 is a novel mechanism of selectivity through the formation of an oxidic particulate, which results in hyper-selectivity.

4.7 Acknowledgements

This work was performed in part at the San Diego Nanotechnology Infrastructure (SDNI) of UCSD, a member of the National Nanotechnology Coordinated Infrastructure, which is supported by the National Science Foundation (Grant ECCS-1542148) and by ASCENT, a Semiconductor Research Corporation (SRC) program. The authors gratefully acknowledge the valuable support of the SRC, Applied Materials who supplied the patterned sample, and EMD who provided the $RuDMBD(CO)_3$ precursor.

Chapter 4, is in part or full, reprinted with permission from S. Wolf, M. Breeden, S. Ueda, J. Woodruff, M. Moinpour, R. Kanjolia, and A. C. Kummel, "The Role of Oxide Formation on Selective Co and Ru ALD" (*manuscript submitted to Applied Surface Science*). The dissertation author was the primary investigator and author of this paper.

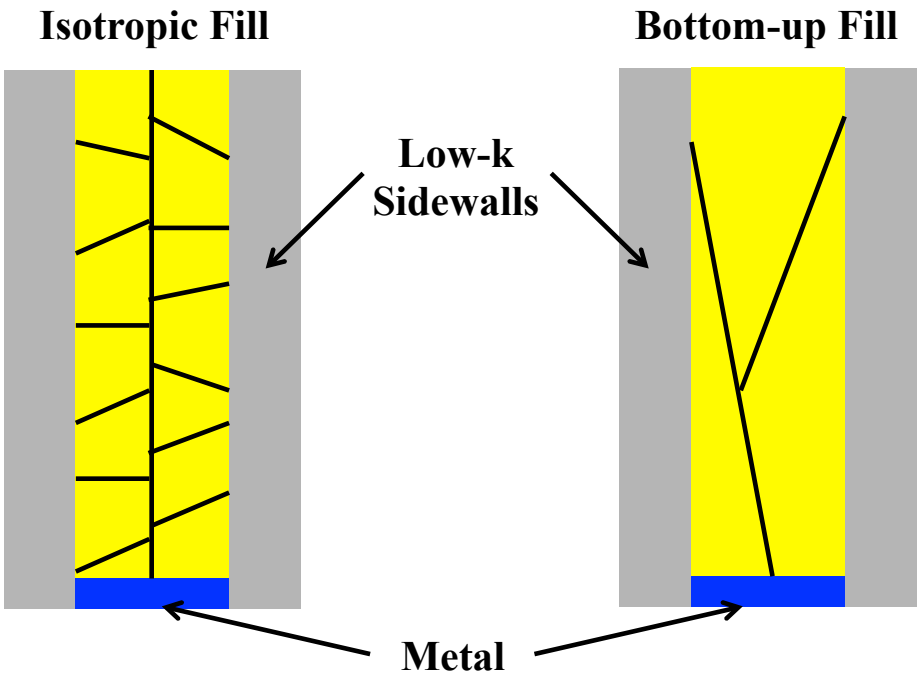

Figure 4.1: Selective Bottom-Up Co. By depositing Co selectively on metals vs. low-k materials during via fill, bottom-up growth can induce the formation of larger grains that provide lower electrical resistance.

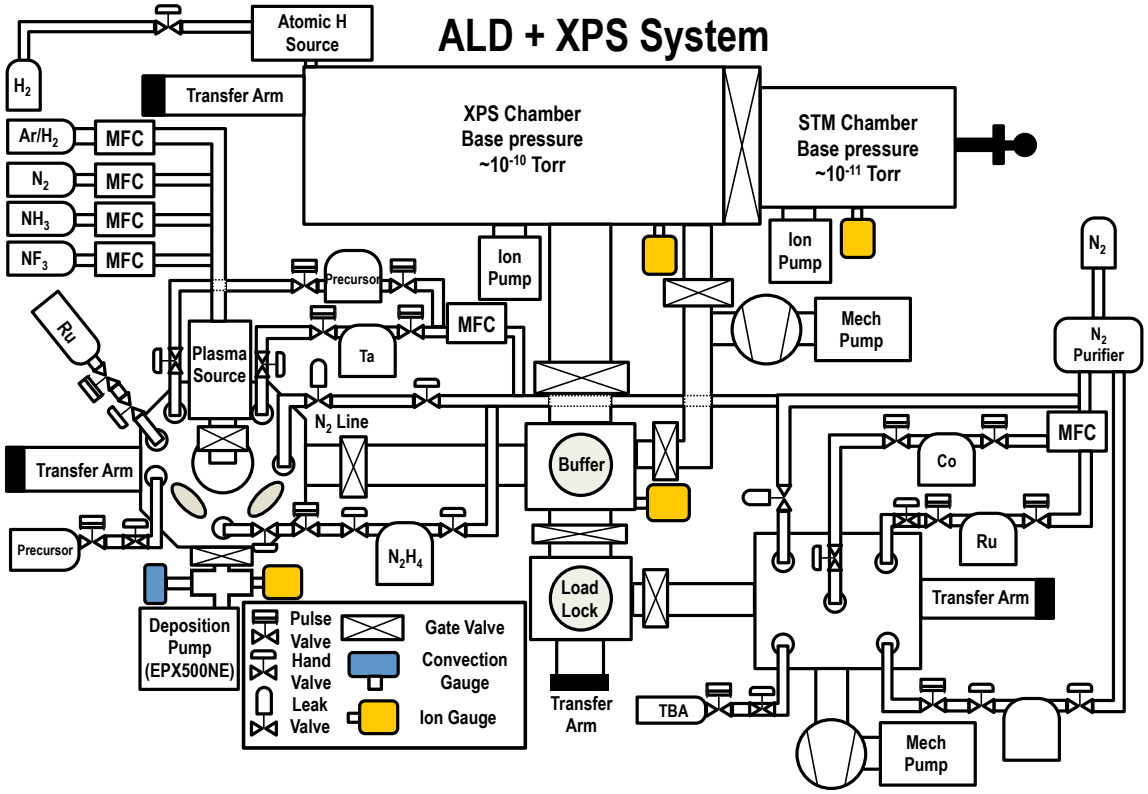

Figure 4.2: Chamber Schematic. An ALD chamber connected *in situ* to the XPS system allows for chemical composition characterization without exposure to ambient conditions. Additionally, a second chamber with an RF downstream plasma source can be used to clean samples with atomic hydrogen.

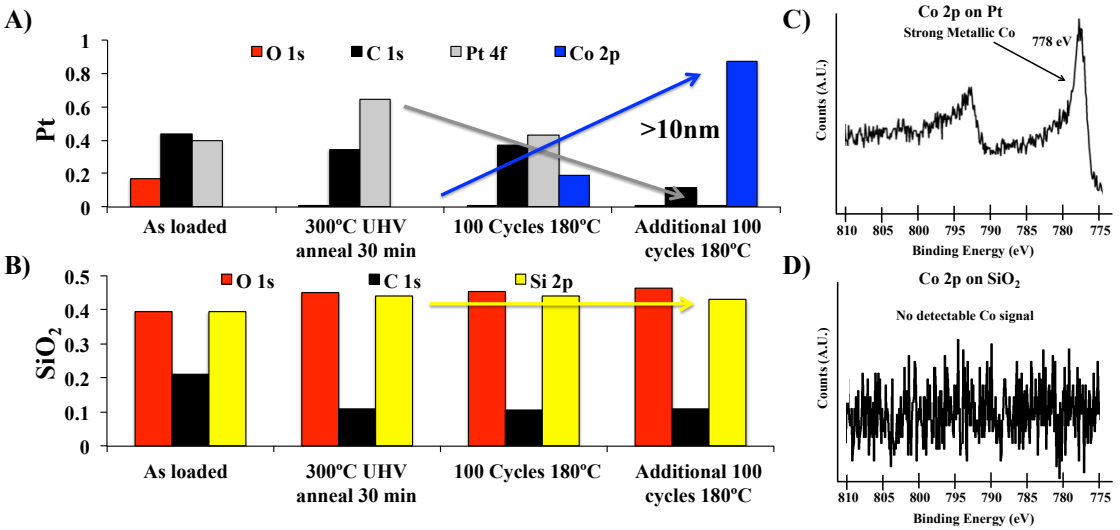

Figure 4.3: XPS of UHV Annealed Substrates that Underwent 100 + 100 Additional ALD Cycles of $Co(dad)_2$ + HCOOH at 180ºC. A) On Pt, a completely buried Pt signal was consistent with a film >10 nm thick. The rapid decrease in the Pt signal (grey) was consistent with a conformal film. B) On SiO_2, the constant Si signal and lack of a Co signal indicated no Co consistent with infinite selectivity. Raw XPS Co 2p spectra showed a strong metallic component on C) Pt, while no observable spectra is observed on D) SiO_2.

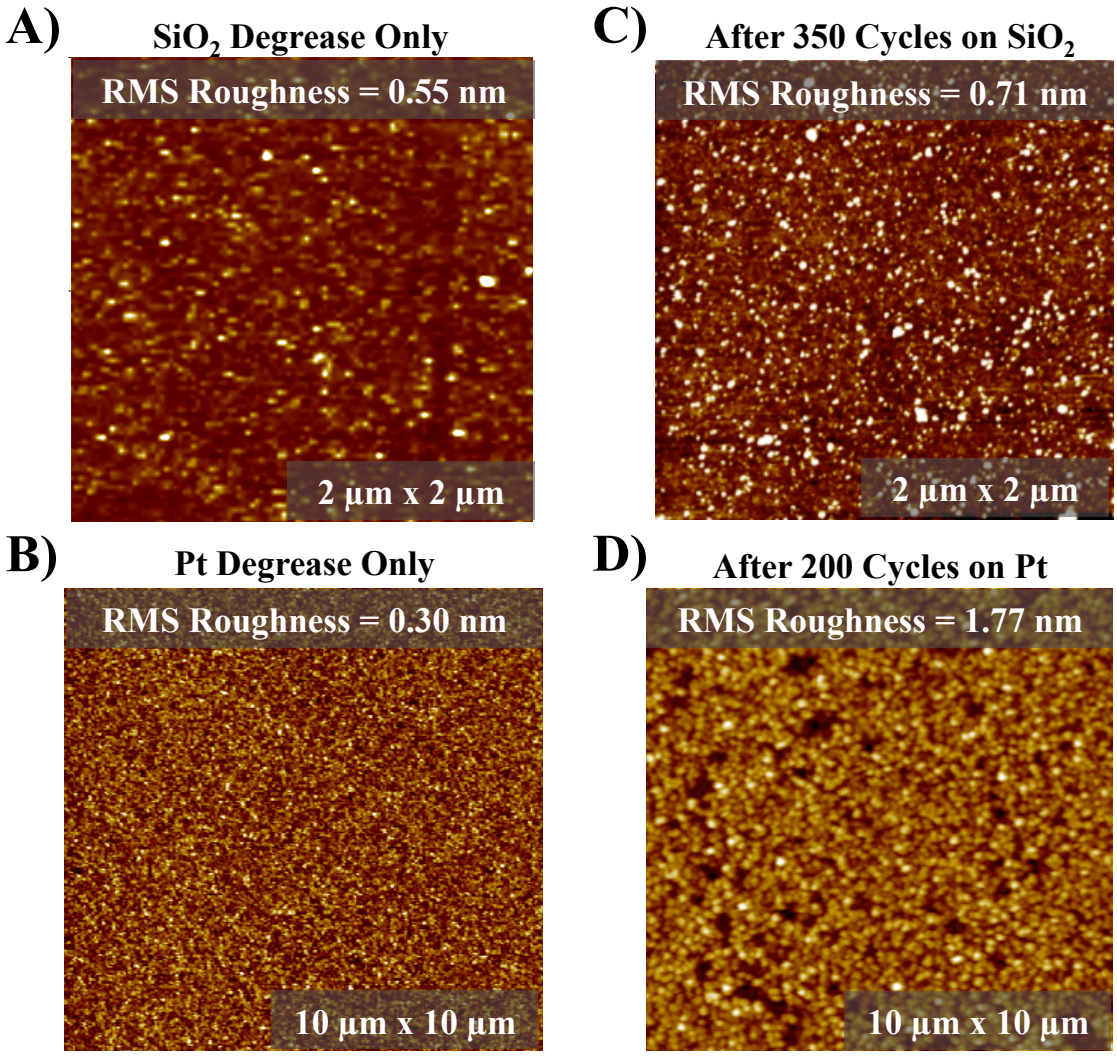

Figure 4.4: AFM Imaging Before and After ALD Cycles on SiO_2 and Pt. On SiO_2, A) before a degrease and C) after cycles, no significant change was observed, while on Pt B) before and D) after deposition surface roughness increased from 0.30 nm to 1.77 nm. Note there was carbon on the starting Pt surface; therefore, plasma cleaning Pt should allow for a more uniform Co film.

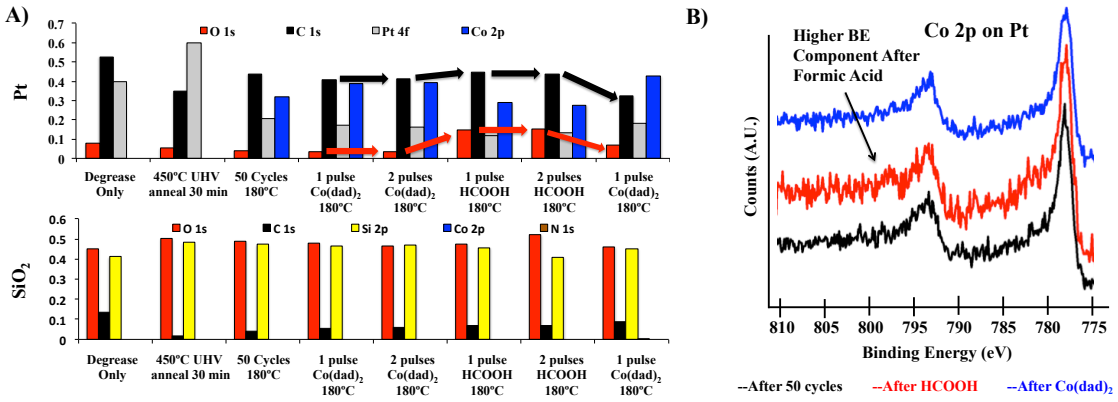

Figure 4.5: Saturation Study of $Co(dad)_2$ and HCOOH at 180ºC. A) The self-limiting exposures were consistent with ALD. The C (black arrows) and O (red arrows) increased after HCOOH dosing suggested a formate was deposited on the surface. The decrease in C and O, and increase in Co, after $Co(dad)_2$ dosing indicated a ligand exchange mechanism for the reaction. B) After HCOOH dosing a higher BE component consistent with a formate deposited on the Co surface. The formate was removed after $Co(dad)_2$ dosing.

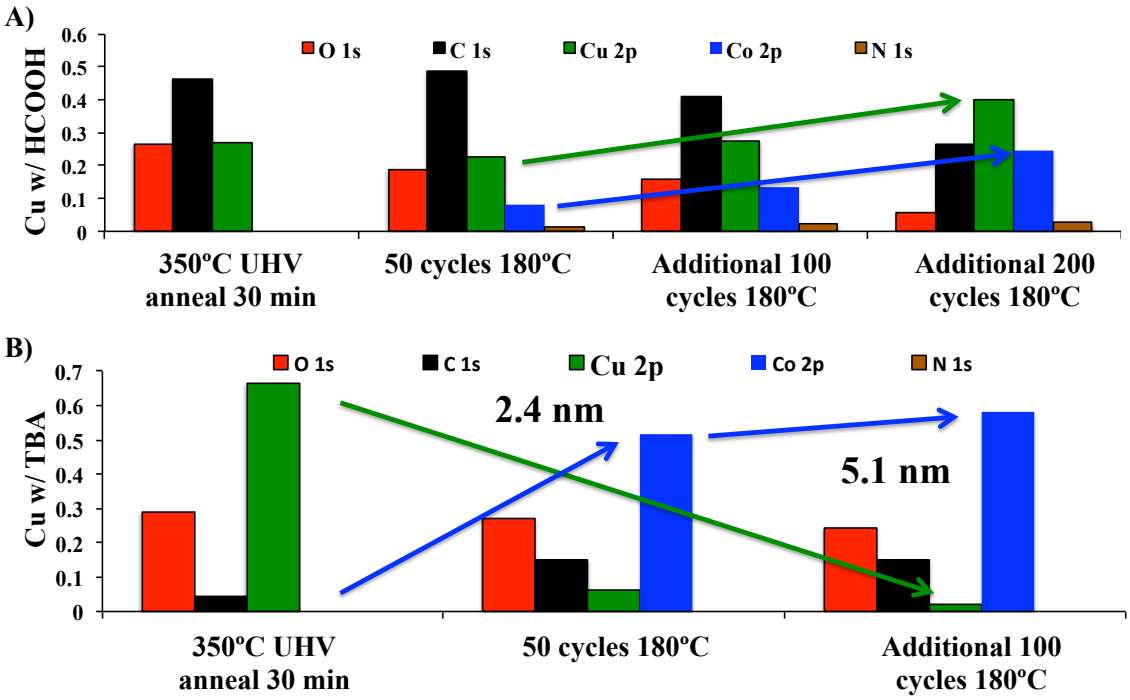

Figure 4.6: Co ALD with $Co(dad)_2$ along with HCOOH vs TBA on Cu. A) No attenuation of the substrate Cu signal (green arrow) with HCOOH was consistent with etching of Cu/CuO_x. B) When ALD was performed with TBA, the Cu fully attenuation (green arrow) consistent with no etching.

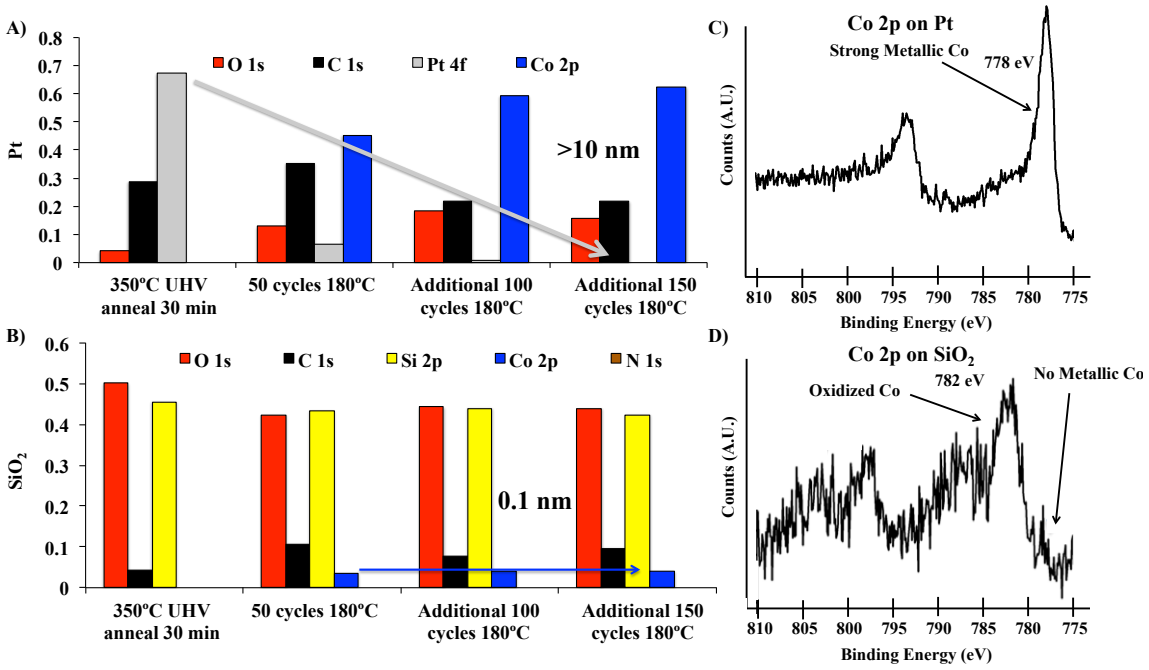

Figure 4.7: Co ALD with $Co(dad)_2$ + TBA on Pt and SiO_2. A) Attenuation of the substrate Pt signal (grey arrow) with TBA was consistent with growing a metallic film on Co from 300 cycles. B) When ALD was performed with TBA on SiO_2, the SiO_2 showed a saturated amount of 4% CoO_x on the surface independent of the number of cycles (blue arrow). The Co 2p raw XPS spectra for growth on C) Pt and D) SiO_2 resulted in an ~4eV difference in binding energy corresponding to metallic vs. oxidized Co deposition, respectively.

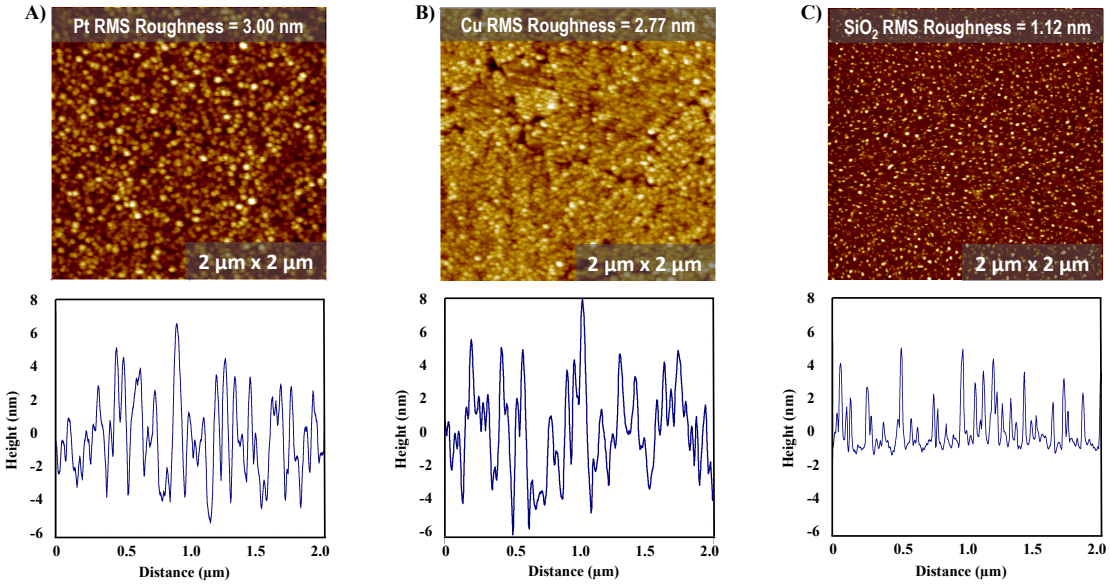

Figure 4.8: Co AFM Imaging and Line Traces of 300 Cycles of ALD with $Co(dad)_2$ along with TBA on Pt, Cu, and SiO_2. A) Pt and B) Cu AFM imaging showed smooth films with low surface roughness. C) Small nuclei consistent with the 4% CoO_x in XPS were detected on SiO_2. The nuclei on SiO_2 were about 2-5 nm tall and about 5-10 nm wide.

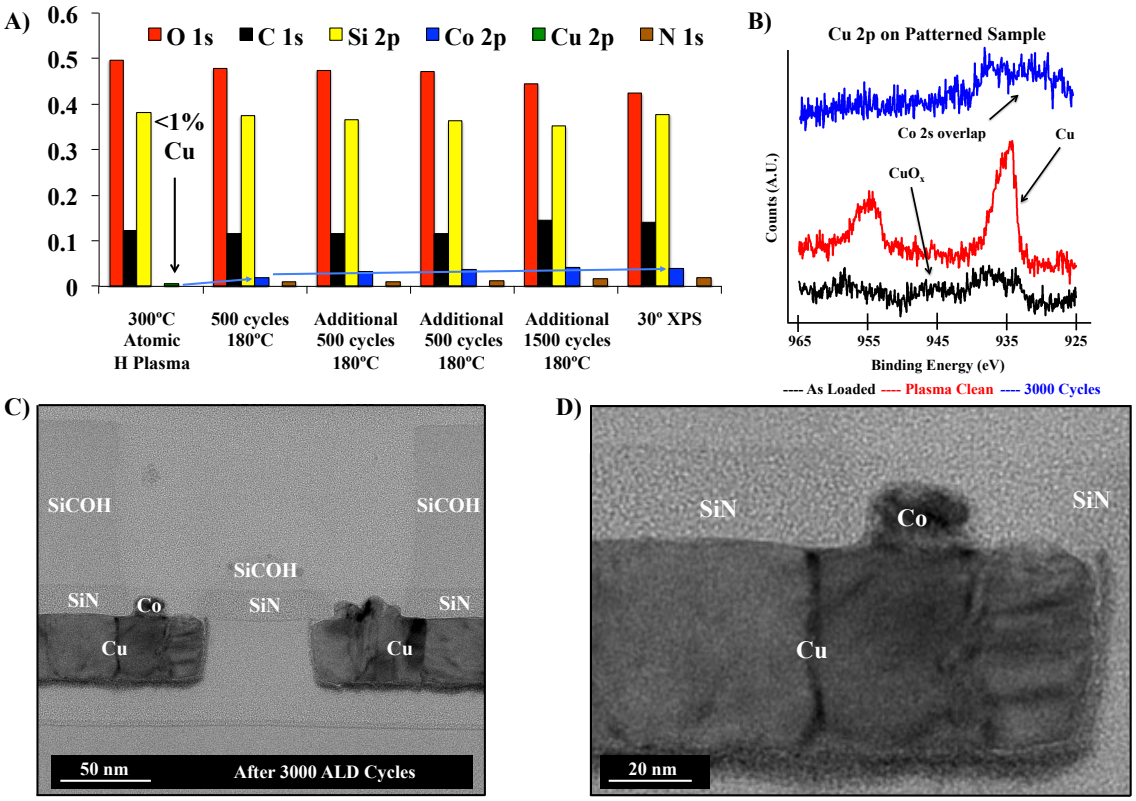

Figure 4.9: Co XPS and TEM of 3000 Cycles of ALD with TBA on Patterned Sample. A) Normalized XPS data indicated Co grew after 500 cycles (blue arrow), but saturated after running additional cycles. B) The Cu 2p peaks became metallic after plasma cleaning and buried after deposition. C) ALD was selective for 3000 cycles against SiCOH and SiN. D) Zoomed-in TEM highlighting ~12 nm Co grown on Cu surface.

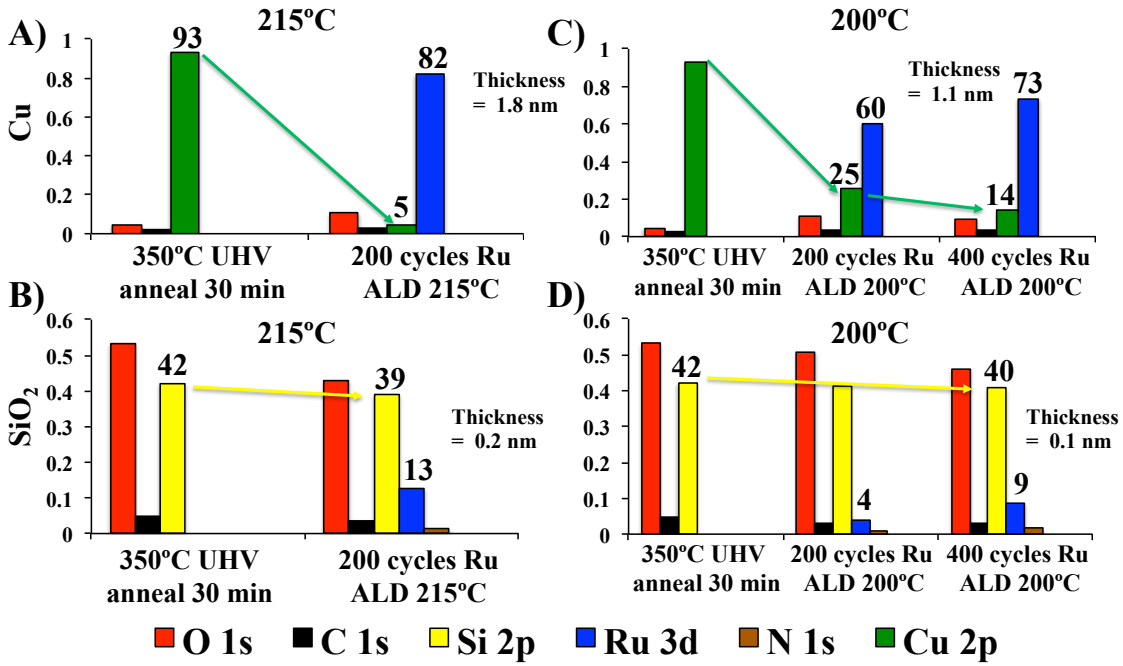

Figure 4.10: Ru XPS on Cu vs SiO_2. At 215ºC, the selectivity of Ru ALD was 1.8 nm on A) Cu (green arrows) vs. 0.2 nm on B) SiO_2 (yellow arrows). Lowering the temperature slightly to 200ºC improved the selectivity on C) Cu vs D) SiO_2, but decreased the growth rate almost a factor of four.

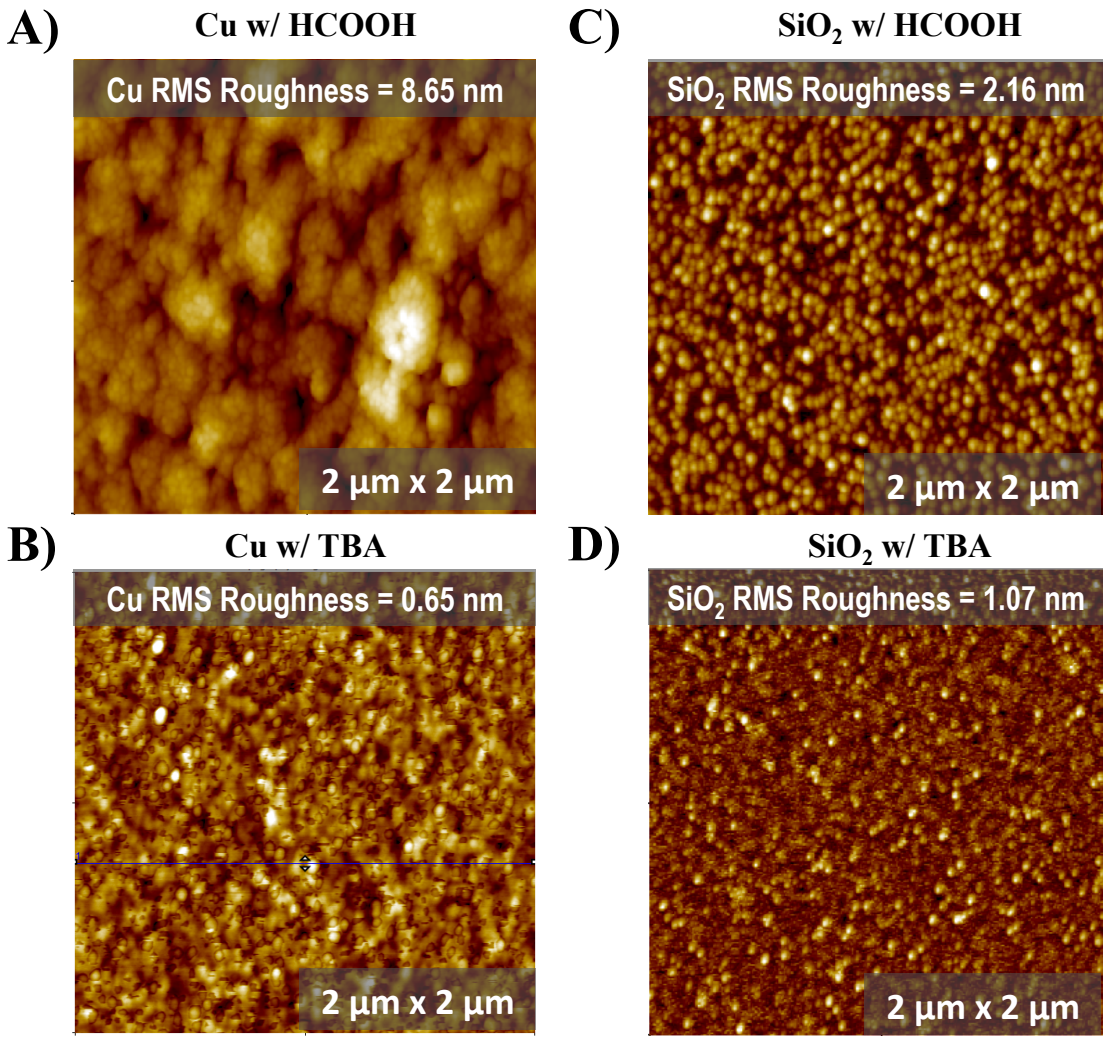

Figure 4.11: Ru AFM on Cu with HCOOH and TBA. Much higher RMS surface roughness was observed from Ru ALD grown with A) HCOOH compared to B) TBA on Cu. Corresponding AFM of Ru grown on SiO_2 using C) HCOOH and D) TBA indicated the RMS surface roughness improved on Cu and SiO_2 by switching to TBA as a co-reactant.

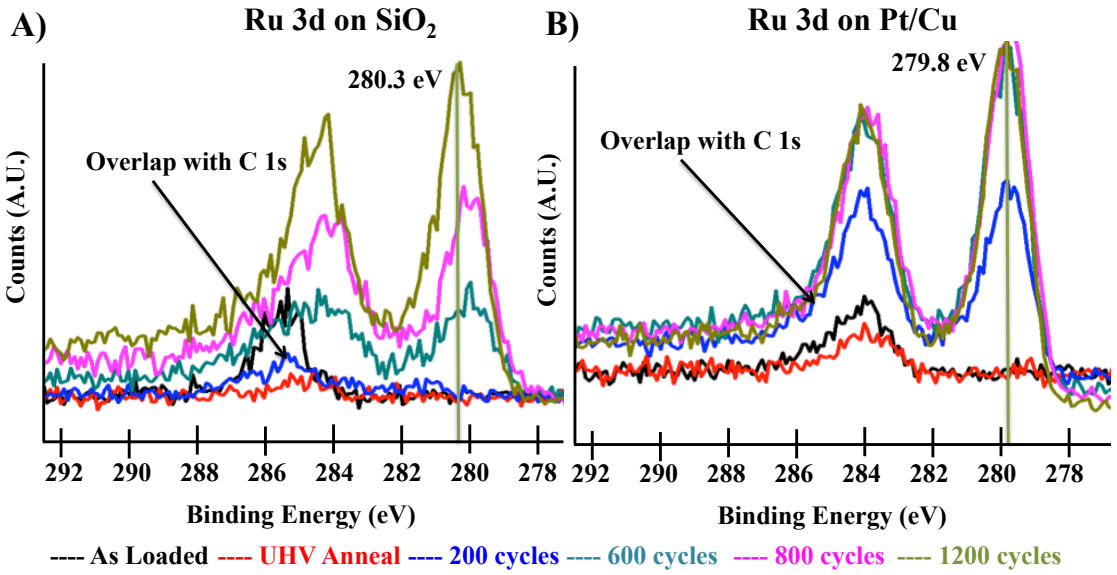

Figure 4.12: Ru 3d raw XPS Peaks. XPS peaks from the as loaded surfaces, after a UHV anneal, and after Ru ALD. The chemical shift of Ru grown on A) SiO_2 vs B) metallic substrates was only about 0.5 eV. This was consistent with a sub-stoichiometric RuO_x depositing on the surface unable to fully inhibit further Ru deposition. Note the small C 1s overlap.

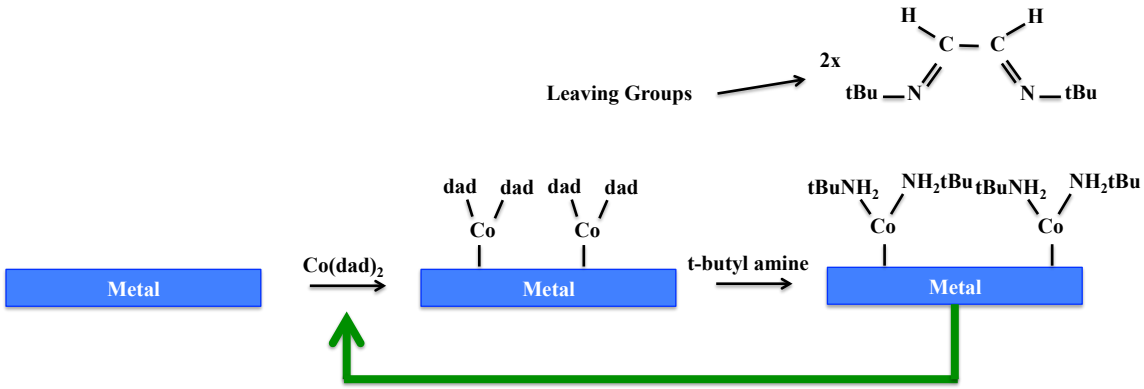

Figure 4.13: Proposed Mechanism for $Co(dad)_2$ + TBA ALD. When $Co(dad)_2$ is exposed to the surface, dad ligands terminate the surface. Following a dose with TBA, the dad ligands are replaced with the amine. The XPS data is consistent with ligand exchange.

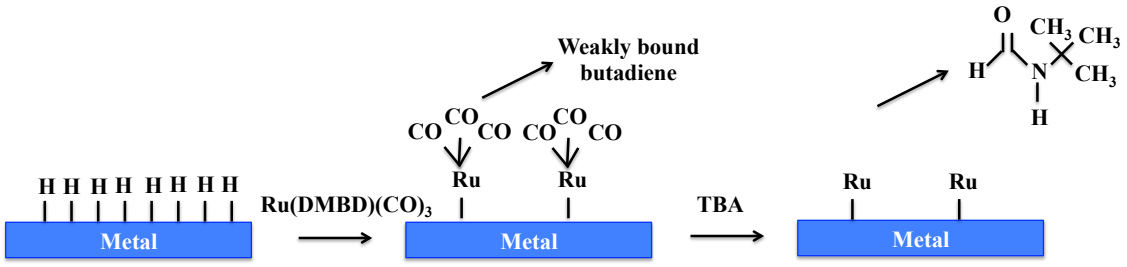

Figure 4.14: Proposed Mechanism for $RuDMBD(CO)_3$ + TBA ALD. When $RuDMBD(CO)_3$ was exposed to the surface the weakly bound butadiene was able to dissociate and volatilize. Following a dose with TBA, the CO ligands were able to react and induce a favorable reaction byproduct leaving metallic Ru on the surface.

4.9 References

1. F. Chen, D. Gardner, Influence of line dimensions on the resistance of Cu interconnections. *IEEE Electron Device Letters* **19**, 508-510 (1998).

2. J. Chawla, F. Gstrein, K. O'Brien, J. Clarke, D. Gall, Electron scattering at surfaces and grain boundaries in Cu thin films and wires. *Physical Review B* **84**, 235423 (2011).

3. B. Feldman, S. Park, M. Haverty, S. Shankar, S. T. Dunham, Simulation of grain boundary effects on electronic transport in metals, and detailed causes of scattering. *physica status solidi (b)* **247**, 1791-1796 (2010).

4. Bekiaris, N., Wu, Z., Ren, H., Naik, M., Park, J.H., Lee, M., Ha, T.H., Hou, W., Bakke, J.R., Gage, M. and Wang, Y., in *2017 IEEE International Interconnect Technology Conference (IITC)*. (IEEE, 2017), pp. 1-3.

5. Wen, L.G., Roussel, P., Pedreira, O.V., Briggs, B., Groven, B., Dutta, S., Popovici, M.I., Heylen, N., Ciofi, I., Vanstreels, K. and Østerberg, F.W., Atomic layer deposition of ruthenium with TiN interface for sub-10 nm advanced interconnects beyond copper. *ACS applied materials & interfaces* **8**, 26119-26125 (2016).

6. C.-C. Yang, P. Flaitz, P.-C. Wang, F. Chen, D. Edelstein, Characterization of selectively deposited cobalt capping layers: Selectivity and electromigration resistance. *IEEE Electron Device Letters* **31**, 728-730 (2010).

7. D. Gall, Electron mean free path in elemental metals. *Journal of Applied Physics* **119**, 085101 (2016).

8. R. Carpio, A. Jaworski, Management of Copper Damascene Plating. *Journal of The Electrochemical Society* **166**, D3072-D3096 (2019).

9. J. P. Klesko, M. M. Kerrigan, C. H. Winter, Low Temperature Thermal Atomic Layer Deposition of Cobalt Metal Films. *Chemistry of Materials* **28**, 700-703 (2016).

10. Kerrigan, M.M., Klesko, J.P., Rupich, S.M., Dezelah, C.L., Kanjolia, R.K., Chabal, Y.J. and Winter, C.H., Substrate selectivity in the low temperature atomic layer deposition of cobalt metal films from bis (1, 4-di-tert-butyl-1, 3-diazadienyl) cobalt and formic acid. *The Journal of chemical physics* **146**, 052813 (2017).

11. Kim, J., Iivonen, T., Hämäläinen, J., Kemell, M., Meinander, K., Mizohata, K., Wang, L., Räisänen, J., Beranek, R., Leskelä, M. and Devi, A., Low-Temperature Atomic Layer Deposition of Cobalt Oxide as an Effective Catalyst for

Photoelectrochemical Water-Splitting Devices. *Chemistry of Materials* **29**, 5796-5805 (2017).

12. M. E. Alnes, E. Monakhov, H. Fjellvåg, O. Nilsen, Atomic layer deposition of copper oxide using copper (II) acetylacetonate and ozone. *Chemical Vapor Deposition* **18**, 173-178 (2012).

13. T. Aastrup, M. Wadsak, C. Leygraf, M. Schreiner, In situ studies of the initial atmospheric corrosion of copper influence of humidity, sulfur dioxide, ozone, and nitrogen dioxide. *Journal of the Electrochemical Society* **147**, 2543-2551 (2000).

14. Austin, D.Z., Jenkins, M.A., Allman, D., Hose, S., Price, D., Dezelah, C.L. and Conley Jr, J.F., Atomic layer deposition of ruthenium and ruthenium oxide using a zero-oxidation state precursor. *Chemistry of Materials* **29**, 1107-1115 (2017).

15. M. H. Hayes, C. L. Dezelah, J. F. Conley, Properties of Annealed Atomic-Layer-Deposited Ruthenium from Ru (DMBD)(CO) 3 and Oxygen. *ECS Transactions* **85**, 743-749 (2018).

16. Gao, Z., Le, D., Khaniya, A., Dezelah, C.L., Woodruff, J., Kanjolia, R.K., Kaden, W.E., Rahman, T.S. and Banerjee, P., Self-catalyzed, Low-temperature Atomic Layer Deposition of Ruthenium Metal Using Zero-valent, Ru (DMBD)(CO) 3 and Water. *Chemistry of Materials*, (2019).

17. Khan, R., Shong, B., Ko, B.G., Lee, J.K., Lee, H., Park, J.Y., Oh, I.K., Raya, S.S., Hong, H.M., Chung, K.B. and Luber, E.J., Area-Selective Atomic Layer Deposition Using Si Precursors as Inhibitors. *Chemistry of Materials* **30**, 7603-7610 (2018).

18. C. Powell, Recommended Auger parameters for 42 elemental solids. *Journal of Electron Spectroscopy and Related Phenomena* **185**, 1-3 (2012).

19. N. McIntyre, M. Cook, X-ray photoelectron studies on some oxides and hydroxides of cobalt, nickel, and copper. *Analytical chemistry* **47**, 2208-2213 (1975).

20. N. McIntyre, D. Johnston, L. Coatsworth, R. Davidson, J. Brown, X-ray photoelectron spectroscopic studies of thin film oxides of cobalt and molybdenum. *Surface and interface analysis* **15**, 265-272 (1990).

21. G. Carson, M. Nassir, M. Langell, Epitaxial growth of Co3O4 on CoO (100). *Journal of Vacuum Science & Technology A: Vacuum, Surfaces, and Films* **14**, 1637-1642 (1996).

22. J. Fuggle, T. Madey, M. Steinkilberg, D. Menzel, Photoelectron spectroscopic studies of adsorption of CO and oxygen on Ru (001). *Surface Science* **52**, 521-541 (1975).

23. C. S. Huang, M. Houalla, D. M. Hercules, C. L. Kibby, L. Petrakis, Comparison of catalysts derived from oxidation of ruthenium-thorium (Ru3Th7) with impregnated ruthenium/thoria catalysts. *The Journal of Physical Chemistry* **93**, 4540-4544 (1989).

24. K. Kim, N. Winograd, X-ray photoelectron spectroscopic studies of ruthenium-oxygen surfaces. *Journal of Catalysis* **35**, 66-72 (1974).

25. J. Shen, A. Adnot, S. Kaliaguine, An ESCA study of the interaction of oxygen with the surface of ruthenium. *Applied surface science* **51**, 47-60 (1991).

26. E. Mercer, D. Farrar, Heats of formation of RuO4, RuO42−, and related compounds. *Canadian Journal of Chemistry* **47**, 581-586 (1969).

27. H. S. C. O'Neill, J. Nell, Gibbs free energies of formation of RuO 2, IrO2, and OsO 2: A high-temperature electrochemical and calorimetric study. *Geochimica et Cosmochimica Acta* **61**, 5279-5293 (1997).

28. Chase, M. W., Curnutt, J. L., Hu, A. T., Prophet, H., Syverud, A. N., & Walker, L. C., JANAF thermochemical tables, 1974 supplement. *Journal of Physical and Chemical Reference Data* **3**, 311-480 (1974).

29. M. M. Minjauw, J. Dendooven, B. Capon, M. Schaekers, C. Detavernier, Atomic layer deposition of ruthenium at 100° C using the RuO 4-precursor and H2. *Journal of Materials Chemistry C* **3**, 132-137 (2015).